Ab Initio Surface Models of Ruthenium Lithium Amide Catalytic Interfaces

Justine Dorival, Jérôme Delmas, David Loffreda

Ab initio Surface Models of Ruthenium Lithium Amide Catalytic Interfaces

Justine Dorival,[†,‡] Jérôme Delmas,[‡] and David Loffreda[*,†]

†*ENSL, CNRS, Laboratoire de Chimie UMR 5182, 46 Allée d'Italie, 69364 Lyon Cedex, France*

‡*Univ. Grenoble Alpes, CEA, Liten, DTNM, 38000, Grenoble, France*

E-mail: david.loffreda@ens-lyon.fr

Phone: +33 (4)72728843

Abstract

Density functional theory calculations are performed to develop atomistic surface models of ruthenium lithium amide catalytic interfaces. In preamble, the stability study of all the $LiNH_2(001)$ terminations demonstrates a preference for NH_2 terminated surfaces with hydrogen pointing toward vacuum and a possibility to reconstruct metastable systems by rotating all the terminal NH_2 moieties. Then, the elaboration of interface models between Ru(0001) and $LiNH_2(001)$ surfaces strongly inspires from a preliminary study of isolated adsorption of lithium and NH_2 on Ru(0001). The competitive adsorption of these species leads to two possible contacts to interface Ru and $LiNH_2$ materials: either through lithium or NH_2. Numerous interface models are optimized by considering the influences of $LiNH_2(100)$ thickness, its stoichiometry and its polarity, including spin polarization and van der Waals interactions. The most stable interfaces are composed of NH_2 planes chemisorbed on Ru(0001). The contact via Li atoms leads to a family of highly metastable interfaces. Surprisingly, the five most competitive interfaces are all non-stoichiometric. The interface stability is then correlated to a Bader charge transfer analysis. This study questions the specific catalytic role of lithium in the context of hydrogen storage and the reaction mechanism of ammonia decomposition on ruthenium lithium amide catalysts.

Introduction

Among future sustainable developments, hydrogen has a key role to play as an energy storage carrier.[1] Indeed, a high industrial impact is expected in various application domains such as energy, environment, automotive and mobile industries, where the dependence towards fossil energies has become a huge worldwide issue. The high energy mass density of hydrogen[2] corresponding to a lower heating value (LHV) at 25°C and 1 bar of 119.7 $MJ.kg^{-1}$ makes this gas molecule very attractive for the energetic storage and decarbonated developments, although its major source of production is strongly dependent on fuels, to date. However, its

extremely low density (0.0824 kg.m^3) at ordinary temperature and pressure conditions results in a low volumetric energy content of 10 MJ.m^3 at ambient conditions and of 8.96 GJ.m^3 for the liquefied H_2 (20.3 K).[2] In comparison, the volumetric energy contents of methane and gasoline are 40 MJ.m^3 and 32 GJ.m^3, respectively. This prevents its massive development as an energy carrier (production and deployment), in part due to storage, toxicity and distribution issues.[1] The industrial reluctance mainly originates from a lack of corresponding infrastructure.[3]

Due to these intrinsic limits related to the direct use of hydrogen as a carrier, alternatives have to be examined to circumvent the major part of these technical difficulties. Among the promising solutions, liquid ammonia presents interesting properties with a high mass fraction of hydrogen[2,4] (17.8 % by weight), a volumetric hydrogen storage density of 120 kg.m^{-3} (about 1.7 times higher than liquid hydrogen, 71 kg.m^{-3}) and a large volumetric energy density[4] (LHV at -33°C and 1 bar of 11.38 GJ.m^{-3}). It is massively produced on the industrial standpoint (Haber-Bosch process, second most produced chemical in the world after sulfuric acid with 183 Mt in 2020). In addition it can be liquefied under mild conditions (8.88 bar at 21°C or -33.5°C at 1 bar), easily stored (with physical properties similar to those of propane meaning that ammonia can be stored in a simple and inexpensive pressure vessel) and already very well distributed, thus making it as an attractive decarbonated hydrogen storage carrier.[4] All these advantages make its utilization interesting in this context, although toxicity risks and energetic costs related to its synthesis and decomposition remain timely. Indeed, high temperature (400-650°C) and pressure (200-400 bar) are required for ammonia synthesis, as well as a high temperature is necessary to decomposition the gas molecule into hydrogen and nitrogen.[3]

In the context of storage and release of hydrogen gas from ammonia carrier, catalytic processes have shown a remarkable route to lower significantly the working temperature. Transition metals such as Fe, Ru and Ni exhibit low apparent activation energies with respect to ammonia decomposition.[2,4] To remedy the cost and stability issues related to monometallics,

multimetallics have been considered in the literature, without showing an equivalent low apparent activation energy barrier.[2] Hence the necessity to explore other families of catalytic materials has led to consider unusual systems such as amides.

Among affordable materials, lithium amides and their derivatives, such as lithium imides and nitrides, have shown relevant properties to store hydrogen.[5] Indeed these materials have been studied and characterized with various experimental techniques, from X-Ray powder[6,7] and neutron powder[7] diffractions, to Raman[7,8] and Infrared[8,9] spectroscopies. The typical size distributions of lithium amide particles correspond to median and mean nanoparticle diameters of 36 and 42 nm, respectively.[6] From Raman spectroscopy, amide and imide groups can be differentiated by the N–H stretching frequency, with distinct bands observed for both amide and imide materials.[7]

From the catalytic standpoint, lithium amide and its interfaces with pure or nitride transition metals[2] have exhibited a convincing and controled way to decompose ammonia into hydrogen and nitrogen. For instance, K-promoted Ru/C and ruthenium-lithium amide based catalysts have demonstrated a remarkable catalytic activity at temperature in the range 350-600°C.[2,3,10,11] Among the best performances, K-promoted Ru/C catalysts have exhibited one of the largest turnover frequency (34 s^{-1}) at 400°C with an apparent activation energy of 139 $kJ.mol^{-1}$.[10] Ni/Al_2O_3 commercial catalyst offers also a competitive performance at 540°C.[2] In addition manganese nitrides interacting with lithium amides have shown a significant turnover frequency (2 s^{-1}) at 465°C with an apparent activation energy of 80 $kJ.mol^{-1}$.[2,12–14]

Lithium amides and related imides alone have also been considered as catalytic materials in the literature for decomposing ammonia, with an interesting performance, according to Makepeace *et al.*'s recent works[15–18] supported by other studies,[19] which are questioned by other measurements showing a less performance,[11–13] and especially at 450°C.[2]

Among the experimental studies comparing various catalysts in similar conditions, Guo *et al.* have shown that $LiNH_2$-Ru/MgO interfacial system outperforms reference pure Ru/MgO,

Ru/CNT and K-Ru/MgO systems, regarding ammonia decomposition in the range 500-700 K.[11] Temperature dependencies of catalytic activities allow to predict an apparent activation energy of 53.2±1.5 kJ.mol^{-1} for $LiNH_2$-Ru/MgO, whereas pure Ru-based catalysts present a barrier in the range 51-89 kJ.mol^{-1}, from Arrhenius plots. According to this study, pure Li_2NH catalyst is significantly less active toward ammonia decomposition with a working temperature range starting from 700 K and a much larger apparent activation energy of 150±2.9 kJ.mol^{-1}. Thanks to X-ray absorption near edge structure (XANES) and extended X-ray absorption fine structure (EXAFS) spectroscopic measurements, $LiNH_2$-Ru interfaces synthesized in this work are composed of metallic ruthenium in contact with $LiNH_2$ materials. FTIR experiments indicate that both $LiNH_2$ and Li_2NH shall be present due to characteristic and detected N-H stretching frequencies. Among the mechanistic assumptions proposed by the coauthors, $LiNH_2$ shall decompose partially into $Li_2NH(Li_{3-x}NH_x)$ species at the interface with ruthenium, with a better performance than ruthenium alone toward NH_3 dissociation, while ruthenium always promotes the formation of nitrogen and hydrogen products. This scenario can be understood as a bifunctional mechanism where lithium amide/imide materials provide easily NH_x species from NH_3 partial dissociation, while ruthenium ensures the formation of the products.

Although many experimental efforts have been devoted over the last twenty years for determining the catalytic performance of ruthenium-based lithium amide catalysts toward the ammonia decomposition, the structure (size, geometry, chemical composition) and energetics of the interfacial region between the metal and the amide is unknown to date, due to a clear lack of characterization *in situ* and *operando*. In addition, since the catalytic site is not really identified yet, the reaction mechanism has to be elucidated, for instance on the basis of the detection of reaction intermediate species.

To go beyond these limits, an interesting approach to improve our understanding of catalytic systems at the atomic scale is the theoretical modeling, which has shown over the years a strong predictive power for the most accurate methodologies such as Density Functional

Theory (DFT).[20–26]

Concerning ammonia synthesis[20,21,23,27–29] and decomposition[24,26,30] on ruthenium extended surfaces and clusters modeled in idealistic condition (vacuum), DFT calculations of NH_3 synthesis on Ru(0001) demonstrate that N_2 dissociation is the rate determining step of the reaction mechanism.[20] Very recently the role of small Ru clusters for achieving ammonia synthesis under mild conditions has been evoked though their structural dynamics.[29] For ammonia dissociation on Ru(0001), the rate determining step is the recombination of adsorbed atomic nitrogen into N_2 product, of which the activation is sensitive to atomic nitrogen surface coverage (E_{act} = 51.0-43.8$\times\theta_N$ kcal.mol^{-1}).[24] This is supported by a more recent theoretical investigation of Ru(0001), Ru(111) and Ir(111) surfaces which has addressed DFT-based temperature-programmed desorption spectra simulations compared to measurements.[26] In addition, a theoretical study reporting on Ru clusters (1-13 atoms) supported on carbon nanotubes has shown the importance of the size effect on the lowering of activation barriers, as well as the key role of interfacial active sites between ruthenium and carbon support.[30]

Lithium amide has been extensively studied in the DFT literature as bulk materials with various computational conditions.[31–37] The ambient temperature and pressure α phase of $LiNH_2$ is a cubic anti-fluorite-like crystal structure with space group $I\bar{4}$ (corresponding to a tetragonal lattice with 32 atoms per unit cell).[38,39] The surfaces and possible terminations of $LiNH_2$ have not been studied in the literature to date, although interesting theoretical models have been proposed for its interface with Li_2NH compound.[40]

In order to model the decomposition of ammonia on Ru/$LiNH_2$ catalyst, Guo *et al.* have reported on a DFT investigation of Li_2NH(110) extended surface model, which is doped by one Ru atom positioned at the surface of the materials.[11] This catalyst model shows a nice ability for adsorbing and dissociating ammonia into NH_2 surface species (thus interesting to regenerate $LiNH_2$ catalyst). However, through the exploration of coupling NH_2-NH and NH-NH aiming to yield N_2 final product of the decomposition, they have predicted large

activation barriers in the range 1.68-1.99 eV, originating from the strong repulsive force between the negatively charged NH_x species. Those barriers are indeed either equivalent to the one on a pure Ru(0001) surface at a nitrogen surface coverage of 0.25 ML (1.70 eV) or larger. Hence the authors have concluded that Li_2NH could not be an efficient catalyst for NH_3 decomposition, due to a recombination step of nitrogen atoms kinetically hindered. Their theoretical result is in good agreement with their experimental findings, showing that Li_2NH alone is not an efficient catalyst for this reaction.[11]

In this work, we report on original density functional theory models of $LiNH_2$ surfaces and $Ru/LiNH_2$ interfaces in the context of ammonia decomposition. Our assumption of considering interface models between metallic ruthenium and $LiNH_2$ comes from previous measurements and characterization for this catalyst.[11] Our objective is the determination of possible active sites for such reaction, by investigating the thermodynamic stability of several interface models between ruthenium and $LiNH_2$ materials, depending on the possible surface terminations of $LiNH_2$. Spin polarized calculations have been performed systematically and the influence of weak van der Waals interactions on the theoretical predictions is also addressed. Two different energy decomposition models have been introduced: the first one for predicting the stability of non-stoichiometric $LiNH_x$ bulk references and the second one for decomposing the interface energy into elementary surface energy contributions.

Methods

All the Density Functional Theory calculations have been performed by the VASP 6.2 package.[41–44] The Generalized Gradient Approximation (GGA) has been considered with the Perdew-Burke-Ernzerhof (PBE) electronic exchange and correlation functional.[45] The standard GGA PBE level has been compared with calculations including weak van der Waals interactions by considering semi-empirical dispersion-corrected functionals in the DFT-D3 Grimme's framework (PBE-D3 with zero damping (0D)[46,47] and Becke-Johnson (BJ)[46,47]

damping function) and in the Steinmann's formalism (PBE-dDsC).[48,49] The Projector-Augmented-Wave approach has been used to describe the core electrons following the Joubert's formalism.[50] Ruthenium atoms have been described with 8 valence electrons and related PAW PBE pseudopotential (electronic configuration $4d^7 5s^1$), while Li atoms have been described with 3 valence electrons ($1s^2 2s^1$), N and H atoms with 5 ($2s^2 2p^3$) and 1 valence electrons, respectively. The extension of the plane basis sets for the description of the valence electrons has been defined with the cut-off energy of 500 eV ($ENCUT = 499.034$ eV for the plane wave basis set and $ENAUG = 628.945$ eV for the plane wave representation of the augmentation charges). The chosen smearing is of the Methfessel-Paxton-type for all systems including Ru metal (bulk, surface and interface), while it is of Gaussian-type for the optimization of lithium amide bulk and surfaces. Due to the presence of amide magnetic fragments in the lithium amide materials, spin-polarization calculations have been performed systematically for all the systems including $LiNH_2$ (bulk, surface, interface). In all the DFT calculations, the criterion of convergence of total electronic energy is 10^{-6} eV, while the one of geometry optimization is ± 0.01 eV.Å^{-1} for the minimization of the residual forces held by the nuclei. The golden rules which ensure converged total electronic energies with respect to the Brillouin zone integration have been determined by increasing progressively the density of the k-point meshes for both ruthenium and lithium amide bulks. For ruthenium bulk, a convergence of total electronic energy below 1 meV has been predicted with a $(35 \times 35 \times 21)$ k-point grid (1320 irreducible k-points). For lithium amide, the same rule has been obtained with a $(15 \times 15 \times 7)$ k-point mesh (228 irreducible k-points). These golden rules hold for all the considered GGA PBE and dispersion-corrected functionals. Note in passing the absence of spin polarization for $LiNH_2$ bulk which is thus non-magnetic. For Li bulk, the BCC structure containing two Li atoms in the unit cell has been optimized for the calculation of the formation energy of $LiNH_2$ bulk with a k-point mesh of $(15 \times 15 \times 7)$. For Ru(0001) clean surface and calculation of surface energies, (1×1) supercells have been modeled with k-point grids of $(35 \times 35 \times 1)$. For the adsorption properties of Li and NH_2 fragment, $(17 \times 17 \times 1)$ k-point

grids have been considered corresponding to the chosen (2×2) supercell. For $LiNH_2(001)$ surfaces, $(15 \times 15 \times 1)$ k-point meshes have been employed to describe the (1×1) supercell. For Ru(0001)-$LiNH_2(001)$ interfaces, $(17 \times 21 \times 1)$ k-point grids have been used to model the $p(2 \times \sqrt{3})R90°$ supercell, also noted $c(2 \times 4)$. For isolated atoms and gas phase molecules (N_2 and H_2) and molecular fragments (NH_2), a gamma-point-only mesh has been considered with large supercells $(15 \times 16 \times 17$ Å$^3)$.

For $LiNH_2$ bulk, the cohesion E_{coh} and formation E_{form} energies, which are addressed in Table 1, have been defined as follows:

$$E_{coh} = \frac{E(LiNH_2(s)) - N(Li) * E(Li) - N(N) * E(N) - N(H) * E(H)}{N_{at}(LiNH_2(s))} \quad (1)$$

where E($LiNH_2$(s)), E(Li), E(N) and E(H) being total electronic energies of $LiNH_2$ stoichiometric bulk, gas phase isolated Li, N and H atoms, respectively; N(Li), N(N) and N(H) being the total numbers of Li , N and H atoms in the $LiNH_2$ stoichiometric bulk, respectively; N_{at}($LiNH_2$(s)) being the total number of atoms in the $LiNH_2$ stoichiometric bulk.

$$E_{form} = \frac{E(LiNH_2(s)) - (N(Li) * E(Li(bulk)) + N(N) * E(N_2) + N(H) * E(H_2))/2}{N_{unit}(LiNH_2(s))} \quad (2)$$

where E(Li(bulk)), E(N_2) and E(H_2) being the total electronic energies of Li BCC bulk, gas phase N_2 and H_2 isolated molecules, respectively; N(N), N(H) and N_{unit}($LiNH_2$(s)), being the total numbers of N atoms, H atoms and $LiNH_2$ units in the $LiNH_2$ stoichiometric bulk, respectively.

The stability of the clean Ru(0001) and $LiNH_2(001)$ surfaces have been determined by evaluating the surface energy as follows. For Ru(0001), the surface energy $\gamma(Ru(0001))$ is calculated by considering the HCP bulk as the reference:

$$\gamma(Ru(0001)) = \frac{E(Ru(0001)) - N(Ru(0001)) * E(Ru)/2}{2 * \mathcal{A}(Ru(0001))} \quad (3)$$

where $E(Ru(0001))$ is the total electronic energy of the relaxed clean Ru(0001) surface, $E(Ru)$ being the total electronic energy of the HCP Ru Bulk (containing 2 atoms in the unit cell), $N(Ru(0001)$ being the total number of Ru atoms in the Ru(0001) slab and $\mathcal{A}(Ru(0001))$ being the surface area of the Ru(0001) model slab.

For $LiNH_2$(001) terminations, the DFT model can be either stoichiometric (s) or non-stoichiometric (ns) (with respect to $LiNH_2$ bulk).

In both cases, the surface energies $\gamma(LiNH_2(001)(\sigma,t_i))$ and $\gamma(LiNH_2(001)(\sigma,t_j))$ of the two terminations t_i and t_j of the stoichiometric ($\sigma = s$) or non-stoichiometric ($\sigma = ns$) slab model are derived as follows:

$$\gamma(LiNH_2(001)(\sigma,t_i)) + \gamma(LiNH_2(001)(\sigma,t_j)) = \frac{E(LiNH_2(001)(\sigma,t_i,t_j)) - E(LiNH_2(\sigma))}{\mathcal{A}(LiNH_2(001))} \tag{4}$$

where $E(LiNH_2(001)(\sigma,t_i,t_j))$ is the total electronic energy of the stoichiometric or non-stoichimoetric slab of $LiNH_2$(001) containing the terminations t_i and t_j, $E(LiNH_2(\sigma))$ being the total electronic energy of the stoichiometric or non-stoichiometric lithium amide bulk and $\mathcal{A}(LiNH_2(001))$ being the surface area of the $LiNH_2$(001) surface model.

The calculation of total electronic energy of the lithium amide bulk (stoichiometric or non-stoichiometric) $E(LiNH_2(\sigma))$ is based on the determination of the elementary interaction pairs between Li atoms $E(Li,Li)$, NH_2 fragments $E(NH_2,NH_2)$ and, Li and NH_2 fragments $\tilde{E}(Li,NH_2)$, obtained on the basis of an energy decomposition analysis (EDA) provided by the calculation of the stoichiometric bulk of $LiNH_2$ (see Table S1 of the Supporting Information for the parameters concerning the additive EDA model). This EDA model has been derived as follows and can be compared to previous theoretical developments:[32]

$$\begin{aligned} E(LiNH_2(\sigma)) = {} & N(Li) * (E(Li,Li) + E(Li)) + N(NH_2) \\ & * (E(NH_2,NH_2) + E(NH_2)) + N(Li,NH_2) * \tilde{E}(Li,NH_2) \end{aligned} \tag{5}$$

where N(Li), N(NH_2), N(Li,NH_2) are the number of Li atoms, NH_2 fragments and of Li-NH_2 chemical bonds, respectively, E(Li) and E(NH_2) being the total electronic energy of Li atom and NH_2 fragments, respectively.

Regarding now the definition of the adsorption energy E^A_{ads} of a Li atom or a NH_2 fragment on Ru(0001), the usual formula has been derived:

$$E^A_{ads} = E(A@Ru(0001)) - E(Ru(0001)) - E(A) \tag{6}$$

where $E(A@Ru(0001))$ is the total electronic energy of the adsorbate A (being Li or NH_2) on a non symmetric Ru(0001) slab, $E(Ru(0001))$ being the total electronic energy of the clean Ru(0001) surface and $E(A)$ being the total electronic energy of an isolated A species in the gas phase (atom for Li and relaxed fragment for NH_2).

The interface energy between Ru(0001) and $LiNH_2$(001) slabs (composed of terminations t_i and t_j) noted $\Gamma(LiNH_2(001)(\sigma,t_i,t_j)@Ru(0001))$ is derived by generalizing the concept of surface energy of these materials. It has thus been calculated by considering Ru and $LiNH_2$ bulks as references, as follows:

$$\begin{aligned}&\Gamma(LiNH_2(001)(\sigma,t_i,t_j)@Ru(0001))\\&=\frac{E(LiNH_2(001)(\sigma,t_i,t_j)@Ru(0001))-(E(LiNH_2(\sigma))+E(Ru))}{\mathcal{A}(LiNH_2@Ru)}\end{aligned}\tag{7}$$

where $E(LiNH_2(001)(\sigma,t_i,t_j)@Ru(0001))$ is the total electronic energy of the interface model between Ru(0001) and $LiNH_2$(001) slabs ($LiNH_2$(001) slab being either stoichiometric or non-stoichiometric with two t_i and t_j terminations) and $\mathcal{A}(LiNH_2@Ru)$ being the surface area of the interface model.

These interface energies can finally be expressed by considering the sum of the surface energies of Ru(0001) (relaxed and non-relaxed for a non-symmetric slab) and of the sum of $LiNH_2$(001) t_i and t_j terminations (energetic costs) balanced by the adhesion energy between materials (energetic gain); the latter term being itself composed by the binding energy between materials (chemical bonding) and the reconstruction energy of $LiNH_2$(001) (a reconstruction which may occur due to the contact with Ru(0001)). Such decomposition has then been derived as follows:

$$\Gamma(LiNH_2(001)@Ru(0001))=\sum\gamma(Ru(0001))+\sum\gamma(LiNH_2(001))+\gamma_{adh}\tag{8}$$

where γ_{adh} is the adhesion energy between both materials normalized by the surface area of the interface model. Those interface energies have been interpreted by evaluating the charge transfer and its variation from the bulk references, through the Bader charge analysis[51–53] at an accurate computational level regarding the charge density and the wavefunction grids.

Results and discussion

Pure Bulk Materials

Before considering the interfaces between ruthenium and $LiNH_2$ materials, the choice of the exchange and correlation electronic functional is examined thanks to the predictions on the corresponding pure bulk materials and their relevance with respect to available measurements. Four functionals have been selected: standard GGA PBE, PBE-D3 (zero damping, noted 0D), PBE-D3 (Becke-Johnson, noted BJ) and PBE-dDsC (the last three functionals including van der Waals interactions through a semi-empirical correction). Regarding crystalline structures, Ru bulk is HCP[54] while $LiNH_2$ is body-centered tetragonal (the low temperature phase being a cubic anti-fluorite-like crystal structure with space group $I\bar{4}$). See Table 1 for details of the measured lattice parameters, Ref.[38,39,55,56] for the crystallographic data of $LiNH_2$, and Figure 1 for an illustration of its bulk structure.

In the case of Ru bulk, the predictions of lattice parameters, cohesion energy and bulk modulus are quite satisfactory at the GGA PBE standard level (see Table 1), with +0.3% and -0.02% of systematic errors from measurements for a and c parameters, respectively, +6.7% for the total cohesive energy in the bulk and +2.3 % for the bulk modulus. Those theoretical results providing a reasonable model for describing the electronic properties in Ru bulk do not suggest the use of a dispersion-corrected functional, since both cohesion energy and bulk modulus are already overestimated with respect to experimental values. In fact, dispersion-corrected functionals are expected to further increase electronic correlation and the binding energy in metals through the inclusion of additional interactions. In addition, the theoretical predictions provided by the GGA PBE functional are known to be much better than those of the hyper-GGA functionals such as HSE06 and PBE0 for Ru bulk, as already demonstrated previously.[57]

This being said, for the description of $LiNH_2$ bulk, the question of long range van der Waals interactions holds, especially between fragments composing the bulk crystalline struc-

ture. Hence dispersion-corrected functionals have also to be tested for Ru bulk, in the perspective of finding the best compromise for studying the interfaces between Ru and $LiNH_2$ materials. For Ru bulk described by van der Waals dispersion-corrected functionals (see Table 1), one can conclude that PBE-D3 (zero damping and Becke-Johnson) functionals do worse for predicting the lattice parameters than standard GGA PBE (-0.5 % for a for both functionals by comparison with measurements, while -0.8 %, -0.7 % for c for both functionals, respectively). The PBE-dDsC functional does not behave similarly, since the prediction on a is slightly improved (-0.2 %) compared to GGA PBE, whereas the one on c is significantly worse (-0.4 %). Regarding cohesion energy, as expected, the three dispersion-corrected functionals do much worse than GGA PBE, to a lesser extent for PBE-dDsC (+12.2 %). For bulk modulus, the impact of van der Waals interactions is negligible. Therefore, if the use of a dispersion-corrected functional is imposed by $LiNH_2$ materials, PBE-dDsC appears as an acceptable compromise for describing Ru bulk properties.

Let us now examine the DFT predictions for $LiNH_2$ bulk materials. Concerning the optimal values of the lattice parameters, the standard GGA PBE functional offers a good description with systematic errors of -0.6 % for a and +0.7 % for c, respectively by comparison with measurements (see Table 1). Moreover, our GGA PBE results are in fair agreement with previous theoretical studies using various codes and computational conditions (LDA, GGA PW91, PBE, PAW, ultrasoft pseudopotentials) where van der Waals interactions were systematically neglected.[31–37] Those reasonable predictions of the crystal structure get worse when dispersion-corrected functionals are considered in the calculations, with a systematic decrease of a and c parameters, compared to GGA PBE. One can conclude that PBE-D3(0D) offers the least worst decrease for a with an error of -2.7 %, whereas PBE-dDsC is the least worst compromise for c with an error of -1.2 %. Hence, not to consider van der Waals interactions would be better regarding crystalline structure, just like Ru bulk.

At the level of energetics, a direct comparison with measurements can not be achieved neither for cohesion energy nor for bulk modulus, due to the lack of experimental data for

$LiNH_2$. However previous theoretical studies have reported on cohesion energies of -3.08 eV/at[32] and 12.086 eV.[37] The first value is compatible with our DFT results from -3.36 eV/at (GGA PBE) to -3.41 eV/at (PBE-D3(BJ)), as reported on Table 1. The second previously reported value also agrees with our computed cohesion energies, when a different normalization is considered (total number of NH_2 fragments or Li atoms, instead of the total number of atoms). As expected the cohesion energy increases when the dispersion correction is considered. PBE-dDsC registers the least increase (-3.37 eV/at) compared to GGA PBE (-3.36 eV/at).

For $LiNH_2$ bulk modulus, our predicted values in the range 24-30 GPa depending on the functional are in fair agreement with a previous study addressing a value of 33 GPa,[32] while being two times lower than another result reported more recently (77.9 GPa[37]). The bulk modulus derivative is quite similar for both Ru and $LiNH_2$ bulk (4.8) and agrees with previous DFT calculations (3.6[37]). The evaluated formation energy of $LiNH_2$ bulk varies from -2.07 to -2.35 eV/$LiNH_2$ (corresponding to -199.6 to -226.6 kJ.mol^{-1}/$LiNH_2$, respectively), depending on the functional (see Table 1). These values agree fairly well with formation enthalpy measurements at 298 K (-1.82 eV or -176 kJ.mol^{-1} [58]) and with previous theoretical predictions at the GGA level (-196.5 kJ.mol^{-1};[31] -212.5 kJ.mol^{-1};[32] -199.2 kJ.mol^{-1};[34] -212.3 kJ.mol^{-1} [36]).

To conclude this analysis concerning the calibration of the DFT approach, we have then decided to keep two functionals for investigating the surfaces and the interfaces of both Ru and $LiNH_2$ materials: GGA PBE offering a good predictive power, both on structure and energetics, and PBE-dDsC as the dispersion-corrected functional exhibiting the least worst deviation with respect to the standard GGA PBE level.

Pure Surfaces

The next important step before generating interfaces between the two materials is the investigation of the DFT models for the pure Ru and $LiNH_2$ surfaces. On the basis of the

two previously selected functionals, we have first examined Ru(0001), as the most stable Ru surface. Symmetric slabs have been considered with various thicknesses in the range 5-13 atomic layers by using the smallest (1×1) supercell. In these models, the three central atomic planes have been kept frozen to the ideal relaxed bulk geometry, while the remaining surface layers have been symmetrically optimized on both sides of the slabs. The vacuum space used to separate two equivalent Ru(0001) slabs along the z axis is 15 Å. By examining the convergence of the surface energy (see Eq. 3) as a function of the slab thickness, an absolute systematic error below ± 0.007 J.m^{-2} is obtained for models with a minimal thickness of 13 layers (see Figure S1 of the Supporting Information). For such thick model, the calculated surface energy of 2.59 J.m^{-2} is in very good agreement with available measurements (2.65 J.m^{-2} as reported in Table 2). In the case of PBE-dDsC, the predicted surface energy of 3.02 J.m^{-2} is larger than the GGA PBE value, in line with the larger bulk cohesion energy discussed previously. This validates once again the choice of the GGA PBE functional. Hence, non-symmetric slabs of Ru(0001) will be considered later in the study with the minimal equivalent thickness of 7 layers.

In the case of $LiNH_2$ materials, the choice of the clean surface in our study has been based on structural mismatch considerations between the *HCP* stacking of Ru and *BCT* crystallinity of $LiNH_2$. The (001) surface selected in this work offers the smallest supercell and minimal structural mismatch when the latter is interfaced with Ru(0001). In fact, $LiNH_2$(001) surface can be modeled with a square (1×1) supercell of length a (5.03 Å from experiments), while Ru(0001) hexagonal structure can be modeled by a rectangular $(2 \times \sqrt{3})$ supercell of lengths 5.40 Å (2×2.70) and 4.68 Å $(\sqrt{3} \times 2.70)$. With structural mismatches of -6.8% and 7.5%, $LiNH_2$(001) is thus a reasonable compromise to elaborate interface models with Ru(0001). In $LiNH_2$(001), the layer stacking offers four different possible terminations, noted T1, T2, T3 and T4, which correspond respectively to the P1, P2, P3 and P4 planes of the bulk structure along the [001] row, as illustrated in Figure 1. According to our notations, T1 termination leads to slabs composed of terminal planes presenting 3 Li atoms,

while T3 termination generates slabs with terminal layers composed of 1 Li atom. In addition, T2 termination leads to slabs with surfaces exhibiting NH_2 fragments oriented toward the materials (the hydrogen atoms defining the convention of orientation and leading to our notation "NH_2 down"), whereas T4 termination leads to slabs with surfaces presenting NH_2 fragments pointing toward vacuum (noted "NH_2 up"). Examples of mixed T1T2 and T3T4 and pristine T1T1, T2T2, T3T3 and T4T4 $LiNH_2(001)$ slabs are presented in Figures 1 and 2. In all our DFT symmetric models of clean $LiNH_2(001)$, the retained supercell is then the (1×1) with a vacuum space of 15 Å. Regarding the thickness of the six considered models, it depends on the considered terminations. For the mixed T1T2 and T3T4 non symmetric slabs, the stoichiometry of $LiNH_2$ bulk is respected and the chosen thickness of our models is 24 planes, as shown in Figure 1 for the initial geometries and Figures S3-S4 of the Supporting Information for optimized structures at both GGA PBE and PBE-dDsC levels. These two models are then defined as stoichiometric and neutral systems. In contrast, for the T1T1, T2T2, T3T3 and T4T4 pristine symmetric slabs, the stoichiometry of $LiNH_2$ bulk can not be respected and the thickness varies from 23 to 25 planes, as illustrated in Figure 2 for starting geometries and Figures S5-S8 for optimized structures at GGA PBE and PBE-dDsC levels. These four latter models of $LiNH_2(001)$ are then non stoichiometric and polar systems, of which the electrostatic potential is convergent, due to a net total dipole moment close to zero, thanks to the slab symmetry. During the geometry optimizations, the models containing T2 terminations (especially T1T2 and T2T2 slabs) with "NH_2 down" configurations at the surfaces, have undergone a surface reconstruction corresponding to a rotation of the NH_2 terminal fragments from a "down" configuration to a "up" position (thus leading to a reconstructed termination noted T4'), as illustrated in the Supporting Information in Figures S3 and S6. Hence, to ensure the optimization of T2 terminations in these cases (non reconstructed systems) and allow the evaluation of their surface energies, we had to freeze the positions of terminal NH_2 fragments in their initial configurations ("NH_2 down"). Similar geometric constraints have also been considered for three other T1T1, T3T4, T4T4

systems, especially to keep the orientation of the NH_2 fragments close to the surfaces. The only system which could be completely relaxed without losing the bulk crystallinity is T3T3. Apart from the necessary geometrical constraints at the terminal planes, all the degrees of freedom of all the other atoms belonging to internal planes have been systematically relaxed in the 5 DFT models of $LiNH_2(001)$ surfaces (T1T2, T3T4, T1T1, T2T2, T4T4). In the Supporting Information, the constrained optimized geometries and the fully relaxed structures presenting reconstructions have been reported in the Figures S3-S8. The relative stability between the four possible terminations of $LiNH_2(001)$ is then determined by calculating the surface energies as introduced in Eq. 4. Conversely to Ru(0001) model, the terminations of $LiNH_2(001)$ models can be either identical (T_iT_i) or different (T_iT_j) in the slabs. This explains the generalization of the equation related to the calculation of surface energies. The symmetric slabs related to the T_iT_i non stoichiometric models allow the evaluation of the surface energy $\gamma(\sigma, t_i)$ of each termination T_i, as soon as the total electronic energy of the non stoichiometric equivalent bulk system ($E(LiNH_2(\sigma))$ is known. To do so, we had to develop an energy decomposition analysis based on stoichiometric bulk model to predict the energy of non stoichiometric bulk systems as explained in the methodology section (see Eq. 5) and in the Supporting Information. In Table 2, the predicted surface energies of the four terminations of $LiNH_2(001)$ have been reported for both GGA PBE and PBE-dDsC functionals. Three terminations (T1, T2 and T4) are magnetic (from 1 to 3 μ_B) while T3 is diamagnetic. We conclude that the lithium terminated slabs T1 and T3 (4.77 $J.m^{-2}$ and 1.53 $J.m^{-2}$, respectively) are less stable than the NH_2 terminated surfaces T2 and T4 (0.35 $J.m^{-2}$ and 0.01 $J.m^{-2}$, respectively) with the GGA PBE functional. This trend is identical at the PBE-dDsC level, as exposed in Table 2. According to these weakly polar symmetric model slabs, the "NH_2 up" terminated surface of $LiNH_2(001)$ is the most stable one with a very weak surface energy for both functionals. Due to the weak polarity of the four symmetric non stoichiometric models of $LiNH_2(001)$, the relevance of the predicted surface energies can be determined from the two other stoichiometric and neutral non symmetric

slabs T1T2 and T3T4. Those two systems allow the evaluation of the sum of two surface energies : $\gamma(\sigma, t_1) + \gamma(\sigma, t_2)$ or $\gamma(\sigma, t_3) + \gamma(\sigma, t_4)$. The calculated values are reported in Table 2. By summing the previously calculated surfaces energies of the four terminations predicted from the symmetric slabs, we calculate the systematic error between the models: 2% (1%) for T1T2 and 6% (5%) for T3T4 at the GGA PBE (PBE-dDsC) level. Since these systematic errors are reasonable with both functionals, the predicted surface energies of $LiNH_2$(001) terminations are thus validated. By the light of this analysis, the interfaces between $LiNH_2$(001) and Ru(0001) exhibiting a termination T4 not in contact with Ru is thus expected to be preferential from the energetic standpoint. This being said, the best choice among the four $LiNH_2$(001) terminations to generate an interface and a contact with Ru can not be easily guessed. To advance on this question, the adsorption properties of Li atom and NH_2 fragment on Ru(0001) have to be investigated in preamble.

Adsorptions on Ru(0001)

For the adsorptions of Li atom and NH_2 fragment, we have chosen to describe the Ru(0001) clean surface by a non-symmetric seven-layer thick slab with a (2×2) supercell (4 Ru atoms per layer). The vacuum space separating two equivalent slabs along the z axis is 15 Å. In our Ru(0001) slab model, the three bottom most atomic layers have been frozen to the ideal relaxed geometry of the Ru HCP bulk (depending on the choice of the functional). The four upmost atomic layers have been totally relaxed. The optimized structures have been presented in Figure 3 and adsorption energetics (see Eq. 6 for definition) and optimal distances in Table 3 at the GGA PBE level. For atomic adsorption of one Li atom, four classical adsorption sites have been considered : onefold top, twofold bridge, threefold hollow HCP and threefold hollow free. The four of them correspond to local minima on the potential energy surface with a slight preference for the two hollow sites (-2.53 eV) with respect to the bridge position (-2.50 eV). The predicted adsorption energy for the best sites is in fair agreement with heat of adsorption measurements[59] (see Table 3), while the calculated Ru-Li distances

at our GGA PBE level are larger than those obtained previously from LDA calculations,[60,61] as expected.

For the adsorption of one NH_2 fragment on Ru(0001), only one structure is found stable (see Table 3 and Figure 3): a twofold bridge position with NH_2 fragment oriented perpendicularly with respect to the Ru-Ru bridge site, in agreement with previous theoretical studies.[21,22,26,28] The top adsorption form is not stable and the NH_2 fragment diffuses spontaneously toward a bridge position during the geometry optimization. The adsorption energy of NH_2 fragment with respect to radical NH_2 gas phase reference is -2.97 eV, thus more exothermic than the energy gain for the best adsorption site for Li atom. The adsorption energetics and optimized geometry are in close agreement with previous DFT calculations[22,26,28] performed with various GGA functionals and surface coverage, as shown in Table 3. Hence, in the perspective of the elaboration of Ru/$LiNH_2$ interface models, the choice of the best termination of $LiNH_2$(001) to be in contact with Ru(0001) is not clear cut at this stage due to the competition between adsorption strengths of Li and NH_2 on Ru(0001). As a consequence, in the following section devoted to those interfaces, the two possibilities of contact between materials will be addressed and compared.

Ruthenium-Lithium Amide Interfaces

In the following section, the DFT models of interfaces between Ru(0001) and $LiNH_2$(001) surfaces will be developed by using the previous results obtained from bulk materials, clean surfaces and adsorption properties. Regarding the calibration of the Ru(0001) slab, we have minimized the computational effort by choosing:

- the smallest supercell which can be interfaced with $LiNH_2$(001) slabs with a minimal structural mismatch : $(2 \times \sqrt{3})$
- the minimal thickness required to have converged surface energy for Ru(0001) : 7 layers (the three bottom most atomic planes being frozen, while the four upmost layers being

totally relaxed, such as the adsorption models exposed in the previous section).

- the vacuum space considered in the interface models is in the range 10-20 Å.

- in all the DFT interface models, the volume of the 3D boxes have not been further relaxed after having set both materials in contact; the optimal parameters of Ru bulk of each functional imposing the size of the 3D boxes due to the much larger rigidity of Ru bulk than the one of $LiNH_2$ material (see the computed bulk moduli in Table 1).

Concerning now the working principles for generating interfaces between materials (see Figure 4), we have ensured that:

- the $LiNH_2(001)$ slabs are interfaced with Ru(0001) by considering both contacts with terminations composed of Li atoms (3 atoms in T1, cf. Figure 4(a) and (b)) and of NH_2 fragments (2 fragments in "NH_2 down" configuration in T2, cf. Figure 4(c) and (d)). The notation of interfaces will thus be $Ru@T_iT_j$, where T_i is in contact with Ru(0001) slab.

- the contacts between $LiNH_2(001)$ and Ru(0001) slabs have been chosen to reproduce as much as possible the most stable adsorption forms of Li atom and NH_2 fragment, as reported in the previous section.

- for the $LiNH_2(001)$ slabs, there are four possible terminations to stop the interface models toward vacuum. For each case, two different $LiNH_2(001)$ thicknesses have been considered to probe the convergence of interface properties. In our interface models, the $LiNH_2(001)$ slab thickness ranges from 9 to 17 (Li or NH_2) planes. At this stage, this leads to 16 possible interface models.

- the $LiNH_2(001)$ slab in the interface can be stoichiometric ($\sigma = s$) (cf. Figure 4(a)) or non-stoichiometric ($\sigma = ns$) (cf. Figure 4(b), (c) and (d)) as previously evoked for $LiNH_2(001)$ surfaces. This slab can be also neutral (n) (cf. Figure 4(a)), polar (p) and

neutralized (nz) either by the adsorption of Li or NH_2 at the contact between materials (cf. Figure 4(b)) or by generating defects such as one or several vacancies (v) related to Li atoms (vLi) (cf. Figure 4(c)) or NH_2 fragments (vNH_2) (cf. Figure 4(d)). When there is no defect or vacancy, the $LiNH_2(001)$ slab is pristine (ps) (cf. Figure 4(a) and (b)).

- to take into account all these possibilities in the notation, we introduce a general name for all our interfaces : $Ru@T_iT_j(N_l, \sigma, p, v)$, where N_l is the number of layers in $LiNH_2(001)$, σ the stoichiometry of $LiNH_2(001)$, p its polarity and v its defect degree.

- the spin polarization is considered in all the interface models.

By using these working principles and corresponding notation, we could have created 25 interface models, of which interface energetics has been addressed in Table 4 and in Figure 5, and of which the optimized structures of the most stable systems have been illustrated in Figure 6. All the illustrations of the optimized interface structures, at both GGA PBE and PBE-dDsC levels, have been reported in the Supporting Information in Figures S9-S20.

After geometry optimization with GGA PBE functional, 10 among 25 interface models keep their initial structural arrangement, at the exception of course of local geometric relaxations, especially in the $LiNH_2(001)$ materials and at the interface with Ru(0001). These systems, which do not undergo a significant reconstruction in the $LiNH_2$ materials, are mentioned as "none" in the corresponding column of Table 4 and they correspond mostly to plain interfaces with no vacancy (except one case Ru@T2T3(14,ns,nz,vLi(cor))). Regarding interface energies, these non-reconstructed systems cover almost the whole range of stability from the most competitive systems (2.37 $J.m^{-2}$ for the Ru@T2T4(9,ns,nz,ps), as illustrated in Figure 6(b)) to the least stable model (12.30 $J.m^{-2}$ for the Ru@T1T1(17,ns,p,ps)). This family of non-reconstructed interfaces is composed of systems with T1 and T2 contacts, with a large preference for T2 contacts.

Among the 25 interfaces, 15 models have undergone a significant reconstruction in the

$LiNH_2$(001) materials (see column 2 of Table 4). 6 systems have undergone a systematic reconstruction in the terminal T2 plane (exposed to vacuum) where the NH_2 fragments have been rotated from a "NH_2 down" configuration toward a "NH_2 up" situation (2 systems being in T1 contact with Ru, and 4 being in T2 contact). Such a reconstruction has thus been noted T4' in our work. This can be explained easily by the energetic gain encountered from T2 to T4 terminations and related surface energies, as reported previously on Table 2. Such a reconstruction is also possible thanks to the free rotations of NH_2 fragments at the terminal plane of the interface models. For a sake of simplicity, the final notations of reconstructed interfaces are kept as identical to those of the initial configurations (see column 1 of Table 4). Concerning interface energies, the two systems in T1 contact with Ru(0001) (plain interfaces) are not competitive in stability with a large interface energy in the range 7.09-7.21 J.m^{-2}, whereas the family of 4 systems presenting a T2 contact and a T4' surface reconstruction (two plain and two defective interfaces containing NH_2 vacancies) constitutes the set of the most stable interfaces with values in the range 1.93-3.13 J.m^{-2} (cf. Figure 6(a),(d)). The most stable interface model predicted in this work Ru@T2T2(11,ns,p,ps) belongs to this family and exhibits a minimal interface energy of 1.93 J.m^{-2} (cf. Figure 6(a)). When the thickness of $LiNH_2$ materials is extended by 4 planes with respect to the most stable system, we have obtained the interface model Ru@T2T2(15,ns,p,ps) (cf. Figure 6(d)) with the same surface reconstruction T2T4' and a very similar layer-by-layer optimized structure. The interface energy is destabilized (2.23 J.m^{-2}) by comparison with the most stable thinner model.

In the remaining 9 interface models presenting a significant reconstruction different from T2T4', 6 systems correspond to defective interfaces only with Li vacancies (both T1 and T2 contacts, with 5 and 1 interface models, respectively), while the 3 remaining ones are plain interfaces with a T2 contact. At the level of interface energies, the 5 defective interface models, with a T1 contact and showing a complex reconstruction, present a much more stable interface energy with respect to their corresponding plain interface model, discussed

before. In other words, the generation of Li vacancies for interface models, with a T1 contact with Ru, leads to more stable systems (in the range 5.83-7.46 J.m^{-2} by comparison with 9.14-12.30 J.m^{-2} for non defective systems). Nonetheless such Li vacancies for defective interfaces with T1 contact do not provide competitive candidates with respect to the most stable system. Regarding the reconstructions, 4 systems, among the corresponding 5 interfaces with a T1 contact, present a complex rearrangement along the $LiNH_2$ materials, in particular at the interface with Ru and at the surface (with vacuum above), with the possibility of merging two different planes composed of Li atoms and NH_2 fragments. Such complex rearrangements have been noted Tij with i and j referencing to P1, P2, P3 or P4 usual planes ($LiNH_2$ bulk). Moreover, two additional notations have been introduced to encounter for half-Li planes ("P5", with two Li atoms, intermediate between P1 and P3) and for half-NH_2 planes ("P6", with one NH_2 fragment instead of 2, such as P2 and P4). i and j follow the initial ordering of the $LiNH_2$ planes along the z axis, from Ru(0001) to the surface terminating $LiNH_2$(001). In this latter family of 6 reconstructed interfaces based on defective systems, the last one Ru@T2T3(10,ns,nz,vLi(cor)) (cf. Figure 6(c)) is by far the most stable one with a low interface energy of 2.42 J.m^{-2}, making this system competitive with respect to the T2T4' family of reconstructed interfaces. Concerning now the family of 3 plain interfaces undergoing a significant reconstruction different from T2T4', they all present a T2 contact with Ru(0001) and complex rearrangements notably at the interface with Ru(0001) and at the surface of $LiNH_2$(001), leading to the formation of P5 and P6 merged planes. These non defective systems are however not much competitive because of large interface energies (in the range 4.10-7.08 J.m^{-2}).

An interesting analysis concerns the discussion of the stability trends of the interface models as a function of the thickness of $LiNH_2$ materials, as depicted in Figure 5(a) at the GGA PBE level. The two families of colored points correspond to the two considered contacts with Ru(0001): T1 contact with black squares and T2 contact with red circles. Among the 13 interface models presenting a T2 contact with Ru(0001), the 8 most stable systems

have been kept, thickness by thickness, from 9 to 16 planes. These 8 systems introduced in Table 4 can be stoichiometric or not, neutral, polar or neutralized, pristine or defective. This family of T2 contact with Ru is the most competitive one regarding their stability. When the $LiNH_2$ thickness increases from 9 to 11 layers, the interface energy becomes minimal with the most stable system at 11 layers (1.93 J.m^{-2}). From 13 to 15 layers, the thicker and equivalent systems describe a similar trend with a global loss of stability (larger interface energy in average). The two singularities at 12 and 16 layers correspond to the same interface model, ending with a surface plane of $LiNH_2$(001) composed of 3 Li atoms (i.e. least stable T1 termination). The interface energies are not competitive at all due to the energetic cost to generate T1 termination. From a more general standpoint, the increase of the $LiNH_2$ materials thickness tends to destabilize the interface energy. Among the 12 interface models related to a T1 contact with Ru(0001), the 8 most stable systems have been also reported in Figure 5(a), from 10 to 17 layers, by keeping the most stable system, thickness by thickness, similarly as T2 contact. The corresponding family of interfaces is globally much less stable than the family presenting a T2 contact with Ru. In addition, when the thickness of $LiNH_2$ materials increases, the interface energy is progressively destabilized in average. As an intermediate conclusion, the contact between Ru(0001) and P2 plane of $LiNH_2$ materials composed of NH_2 fragments leads to more favorable interfaces. This result is by far counter-intuitive with respect to the DFT calculations comparing Li and NH_2 adsorption on Ru(0001). Moreover the thinner the extent of $LiNH_2$(001) slab in the interface with Ru(0001), the more stable is the interface. The 4 most stable interface models belonging to the family of T2 contact with Ru(0001) exhibit an interface energy in the range 1.93-2.42 J.m^{-2}, which is lower than the calculated surface energy of clean Ru(0001) surface (2.59 J.m^{-2} at GGA PBE level). This means that these interface models are more stable than the clean metallic surface, so the T2 contact with $LiNH_2$(001) is thermodynamically favorable. Hence this latter comparison justifies the relevance of our choices for the interface models.

At the level of magnetism, the spin polarization predicted for the most stable interface models, thickness by thickness, discussed before, have been reported in Figure 5(b) at the GGA PBE level, by keeping the correspondence of color labeling. As addressed in the Methodology section, all the interface models have been optimized with spin-polarized calculations. According to the total magnetization obtained as a function of the contact between $LiNH_2$ and Ru, and as a function of the thickness of $LiNH_2$ materials in the interface model, no clear trend is observed. The evolution of spin properties is by far complex (with non magnetic, weakly and strongly magnetic systems) and justifies the exigence of considering magnetization throughout the study.

In order to go further in the understanding of the absolute stability of the considered interface models, one can decompose the interface energies into the sum of surface energies to form the two separate materials slabs put in contact (positive and destabilizing contribution) and the adhesion energy corresponding to the energetic gain (negative and stabilizing contribution) related to the chemical bonding between materials and the likely reconstruction at the terminations of $LiNH_2$(001) slab if it occurs (see Eq. 8). According to the previous analysis, the most stable family of interfaces exhibits a T2 contact with Ru(0001) and corresponds to non-stoichiometric, polar or neutralized systems (neutralization either by contact with Ru or via the generation of vacancies), pristine or defective, if we keep the five most competitive systems having an interface energy in the range 1.93-2.50 J.m^{-2} at the GGA PBE level. None of these interfaces are stoichiometric and neutral with respect to $LiNH_2$(001) slab, such as Ru@T2T1(12,s,n,ps) or Ru@T2T1(16,s,n,ps). This is then counter-intuitive to favor complex interfaces as those belonging to the most stable family. The absolute stability of the most stable system Ru@T2T2(11,ns,p,ps) (1.93 J.m^{-2}) results from a significant energetic cost to form $LiNH_2$(001)˙T2T2 and Ru(0001) slabs (5.99 J.m^{-2}) and the counter-balancing energetic gain due to adhesion (-4.05 J.m^{-2}), according to Table 4. By increasing the thickness of the $LiNH_2$(001) slab, we obtain a similar Ru@T2T2(15,ns,p,ps) system, which is however less stable than the thinner equivalent system, because of a weakening of the adhesion energy

(-3.76 J.m^{-2}), the cost for generating the slabs being identical. In fact, $LiNH_2$(001) has a weaker propensity to accommodate the structural mismatch with the Ru(0001) surface for thicker slabs due to the larger cohesion energy in its crystal at GGA PBE. By decreasing the thickness of $LiNH_2$(001) from the most stable system Ru@T2T2(11,ns,p,ps), one generate a non stoichiometric neutralized interface model Ru@T2T4(9,ns,nz,ps), which combines two intrinsic qualities : the spontaneous loss of polarity due to the T2 contact with Ru(0001) and the minimal energetic cost to form $LiNH_2$(001)˙T2T4 and Ru(0001) slabs (5.65 J.m^{-2}). However, as reported in Table 4, the adhesion energy is less stabilizing (-3.28 J.m^{-2}), hence showing the benefit of the T2T4' reconstruction (estimated to -0.77 J.m^{-2}), in the case of the most stable system (with an adhesion energy of -4.05 J.m^{-2}). For Ru@T2T4(9,ns,nz,ps), the increase of the thickness of $LiNH_2$ leads to similar conclusions (destabilizing of interface energy due to a weakening of adhesion energy). Finally, the generation of one Li vacancy results in a fifth competitive interface model Ru@T2T3(10,ns,nz,vLi(cor)) with an interface energy of 2.42 J.m^{-2}. This defective system has a better ability to minimize the structural mismatch with Ru(0001) (more exothermic adhesion energy of -4.75 J.m^{-2})) at the detriment of a much larger energetic cost to form $LiNH_2$(001)˙T2T3 and Ru(0001) slabs (7.17 J.m^{-2}), due to the larger surface energy of T3 termination composed of one Li atom. In summary, Ru@T2T2(11,ns,p,ps) is the most stable interface model since it combines a minimal cost to generate both slabs to put in contact with a significant energetic gain related to adhesion energy. Regarding now the other less competitive systems presenting a T2 contact with Ru(0001), the interface energies are larger due either to the presence of NH_2 vacancies which diminishes the adhesion energy or to the presence of T1 or T3 terminations in the $LiNH_2$(001) slab leading to a much larger energetic cost to form it. The worst cases correspond to the stoichiometric and neutral systems Ru@T2T1(12,s,n,ps) and Ru@T2T1(16,s,n,ps) exhibiting the largest cost to form the slabs (10.40 J.m^{-2}). For the same reasons, all the interface models involving a T1 contact with Ru(0001) imply a much larger interface energy, because of a high energetic cost to generate the two slabs (in the range 10.06-14.82 J.m^{-2}). Such a cost

is never counter-balanced by the adhesion energy and even the T1 contact with Ru(0001) through 3 Li atoms may be more favorable (with adhesion energies up to -8.85 J.m^{-2}).

The whole energetic analysis has been extended to the DFT calculations including dispersion (van der Waals forces) thanks to the PBE-dDsC functional (see the methodology section). Due to the weak competition of interface models involving a T1 contact with Ru(0001) at the GGA PBE level, only the 12 interface models presenting a T2 contact with Ru have been reoptimized with PBE-dDsC and the corresponding results are exposed in Table 4 and in the Supporting Information for optimized geometries. By the light of these complementary results, our conclusions drawn from GGA PBE calculations have been confirmed (at the exception of the effect of $LiNH_2$(001) thickness), thus showing the robustness of our theoretical approach (the interface energies being similar between functionals).

The stability of the interfaces between both materials can be related to an electronic analysis based on Bader charge transfers, as reported in Figure 7. For the separate Ru(0001) and $LiNH_2$ bulk systems, the Bader charge analyses (see Figure 7(a)) show that the two surface layers of clean Ru(0001) have gained electrons at the detriment of the two subsurface layers which are positively charged, while the $LiNH_2$ bulk (see Figure 7(b)-(d)) exhibits a distribution of charges in agreement with the electronegativity of atoms and fragments (Li atoms being positively charged, while NH_2 moities being negatively charged, and the charges being hold by N atoms). For the most stable interface model Ru@T2T2(11,ns,p,ps), the contact between materials induces a charge transfer from the surface layer of Ru(0001) (see Figure 7(a)), in contact with lithium amide, to the internal NH_2 planes of $LiNH_2$(001), as illustrated in Figure 7(c). Hence the initially available negative charge at the surface of Ru(0001) is transfered to the core of $LiNH_2$(001). Moreover, all the Li and H atoms (positively charged) are spectator in such charge transfer due to the interfacing. The generation of a NH_2 single vacancy at the core of $LiNH_2$(001) interfaced with Ru(0001) leads to a significant destabilization of the interface (see for instance Ru@T2T2(11,ns,nz,vNH_2(cor))). The Bader charge transfer is less for this defective and neutralized system than the one previously

discussed for the most stable interface model. Hence there is a correlation between the Bader charge transfer and the stability of the catalytic interface. At the opposite, in the case of the most stable interface between materials with a T1 contact (Ru@T1T2(12,s,n,ps) which is by far less stable than the majority of interfaces with a T2 contact), we obtained a charge transfer from $LiNH_2(001)$ to the interface with Ru(0001), which is characterized by an electronic depletion of the N atoms belonging to the terminal plane of $LiNH_2(001)$ composed of a reconstructed T4' termination (NH_2(up)) and concomitant significant electronic gains at the interface between Ru(0001) and $LiNH_2(001)$, especially at the surface layer of Ru(0001), at the adsorbed Li atomic plane and at the NH_2 plane closest to the interface. Finally the counter-intuitive and opposite charge transfer from $LiNH_2(001)$ to Ru(0001) in the case of a T1 contact explains the high metastability of such interfaces.

Conclusion

In this study, we have exposed DFT calculations of clean $LiNH_2(001)$ surfaces, adsorption properties of atomic Li and NH_2 fragment on Ru(0001) as well as interface models for the Ru(0001)/$LiNH_2(001)$ catalyst, with various exchange-correlation functionals and a systematic description of spin polarization. Although the standard GGA PBE functional provides a satisfactory level of predictions for separate Ru and $LiNH_2$ bulk materials, the consideration of van der Waals forces has also been explored in this work, showing a less predictive power concerning structure and energetics of bulk materials. Among the dispersion-corrected functionals, PBE-dDsC has been selected as the best compromise for describing weak van der Waals interactions without deviating too much with respect to the satisfactory GGA PBE level. Regarding Ru(0001)/$LiNH_2(001)$ interfaces, a large set of possibilities has been explored by varying the chemical contact between both materials, the thickness of the $LiNH_2(001)$ slab, its stoichiometry and its polarity. Five interface models have shown a remarkable stability with an interface energy lower than the surface energy of the clean

Ru(0001) surface. This means that the absolute stability of those five interfaces is intermediate between the high stability of $LiNH_2$(001) most stable termination (NH_2 terminal planes with hydrogen atoms pointing toward vacuum) and Ru(0001). Hence the contact between Ru and $LiNH_2$ materials induces a significant loss of stability for $LiNH_2$ moiety which can compensate this by structural reconstructions. These reconstructions can be all the more important than $LiNH_2$ is defective with the presence of vacancies. Our theoretical models show that the contact between Ru(0001) and a NH_2 terminal plane of $LiNH_2$(001) is much more favored than the one between Ru(0001) and a Li terminal plane of $LiNH_2$(001). The five most competitive interfaces are all non stoichiometric, polar or neutralized, pristine or defective with the presence of one single lithium vacancy. The stoichiometric interfaces are particularly high in energy. The most frequent reconstruction which has been registered in all the interface models corresponds to a rotation of the terminal NH_2 plane from a bulk configuration oriented toward $LiNH_2$(001) to a conformation where the hydrogen atoms of NH_2 fragments are pointing toward vacuum. The corresponding energy gain has been evaluated to -0.77 J.m^{-2}.

This theoretical study opens interesting perspectives for developing relevant interface models in the context of the decomposition of ammonia on Ru/$LiNH_2$ catalyst. Thanks to the particular interfacial structure between both materials, several assumptions could be postulated for elucidating the reaction mechanism. Since the most stable candidates for interfacing Ru and $LiNH_2$ materials are composed of a contact through NH_2 fragments, the role of lithium atoms present in the amide could be either indirect, i.e. at distance from the transition state of the rate determining step (through an electrostatic control), or direct by generating new lithiated surface species (through an orbitalar control).

Acknowledgement

The authors thank PSMN in Lyon and GENCI national resources (IDRIS, CINES, TGCC, project 609) for CPU time and assistance. The authors thank the CPER/SYSPROD 2015-2022 project (N°2019-AURA-P5B) and AXELERA Pôle de Compétitivité (PSMN Data Center). Justine Dorival thanks CEA/LITEN for the PhD fellowship. All authors thank CEA for financial support and CNRS (convention de collaboration CEA:C41048-CNRS:245670).

Supporting Information Available

- Figure S1 illustrating the convergence of surface energy for Ru(0001) as a function of the slab thickness.
- Figure S2 illustrating the convergence of the surface energies for $LiNH_2$(001) terminations as a function of the slab thickness.
- Equation presenting the additive model aiming to predict the total electronic energy of any stoichiometric and non-stoichiometric bulk of $LiNH_2$, which is useful for determining surface energies of $LiNH_2$(001) terminations and interface energies of Ru(0001)/$LiNH_2$(001).
- Table S1 presents the two-body interaction energy terms (Li-Li, NH_2-NH_2, Li-NH_2) at the GGA PBE and PBE-dDsC levels.
- Figures S3-S8 illustrating lateral views of optimized structures of the 6 $LiNH_2$(001) surface models: T1T2, T3T4, T1T1, T2T2, T3T3, T4T4 (at both GGA PBE and PBE-dDsC levels). Constrained and reconstructed surface models are both presented.
- Figures S9-S20 illustrating lateral views of the optimized structures of the complete set of Ru(0001)/$LiNH_2$(001) interfaces (at both GGA PBE and PBE-dDsC levels).

References

(1) Christensen, C. H.; Johannessen, T.; Sørensen, R. Z.; Nørskov, J. K. Towards an ammonia-mediated hydrogen economy? *Catalysis Today* **2006**, *111*, 140–144.

(2) Lucentini, I.; Garcia, X.; Vendrell, X.; Llorca, J. Review of the Decomposition of Ammonia to Generate Hydrogen. *Industrial & Engineering Chemistry Research* **2021**, *60*, 18560–18611.

(3) Chen, C.; Wu, K.; Ren, H.; Zhou, C.; Luo, Y.; Lin, L.; Au, C.; Jiang, L. Ru-Based Catalysts for Ammonia Decomposition: A Mini-Review. *Energy & Fuels* **2021**, *35*, 11693–11706.

(4) Wan, Z.; Tao, Y.; Shao, J.; Zhang, Y.; You, H. Ammonia as an effective hydrogen carrier and a clean fuel for solid oxide fuel cells. *Energy Conversion and Management* **2021**, *228*, 113729.

(5) Garroni, S.; Santoru, A.; Cao, H.; Dornheim, M.; Klassen, T.; Milanese, C.; Gennari, F.; Pistidda, C. Recent Progress and New Perspectives on Metal Amide and Imide Systems for Solid-State Hydrogen Storage. *Energies* **2018**, *11*.

(6) Baldissin, G.; Boag, N. M.; Tang, C. C.; Bull, D. J. Synthesis of Pure Lithium Amide Nanoparticles. *European Journal of Inorganic Chemistry* **2013**, *2013*, 1993–1996.

(7) Makepeace, J. W.; David, W. I. F. Structural Insights into the Lithium Amide-Imide Solid Solution. *The Journal of Physical Chemistry C* **2017**, *121*, 12010–12017.

(8) Bohger, J.-P.; Eßmann, R.; Jacobs, H. Infrared and Raman studies on the internal modes of lithium amide. *Journal of Molecular Structure* **1995**, *348*, 325–328.

(9) Kojima, Y.; Kawai, Y. IR characterizations of lithium imide and amide. *Journal of Alloys and Compounds* **2005**, *395*, 236–239.

(10) Raróg, W.; Kowalczyk, Z.; Sentek, J.; Składanowski, D.; Szmigiel, D.; Zieliński, J. Decomposition of ammonia over potassium promoted ruthenium catalyst supported on carbon. *Applied Catalysis A: General* **2001**, *208*, 213–216.

(11) Guo, J.; Chen, Z.; Wu, A.; Chang, F.; Wang, P.; Hu, D.; Wu, G.; Xiong, Z.; Yu, P.; Chen, P. Electronic promoter or reacting species? The role of LiNH2 on Ru in catalyzing NH3 decomposition. *Chem. Commun.* **2015**, *51*, 15161–15164.

(12) Guo, J.; Wang, P.; Wu, G.; Wu, A.; Hu, D.; Xiong, Z.; Wang, J.; Yu, P.; Chang, F.; Chen, Z. et al. Lithium Imide Synergy with 3d Transition-Metal Nitrides Leading to Unprecedented Catalytic Activities for Ammonia Decomposition. *Angewandte Chemie International Edition* **2015**, *54*, 2950–2954.

(13) Guo, J.; Chang, F.; Wang, P.; Hu, D.; Yu, P.; Wu, G.; Xiong, Z.; Chen, P. Highly Active MnN–Li2NH Composite Catalyst for Producing COx-Free Hydrogen. *ACS Catalysis* **2015**, *5*, 2708–2713.

(14) Chang, F.; Guo, J.; Wu, G.; Wang, P.; Yu, P.; Chen, P. Influence of alkali metal amides on the catalytic activity of manganese nitride for ammonia decomposition. *Catalysis Today* **2017**, *286*, 141–146.

(15) Makepeace, J. W.; Wood, T. J.; Hunter, H. M. A.; Jones, M. O.; David, W. I. F. Ammonia decomposition catalysis using non-stoichiometric lithium imide. *Chem. Sci.* **2015**, *6*, 3805–3815.

(16) Wood, T. J.; Makepeace, J. W.; David, W. I. F. Isotopic studies of the ammonia decomposition reaction using lithium imide catalyst. *Phys. Chem. Chem. Phys.* **2017**, *19*, 4719–4724.

(17) Wood, T. J.; Makepeace, J. W. Assessing Potential Supports for Lithium Amide-imide Ammonia Decomposition Catalysts. *ACS Applied Energy Materials* **2018**, *1*, 2657–2663.

(18) Makepeace, J. W.; Brittain, J. M.; Sukhwani Manghnani, A.; Murray, C. A.; Wood, T. J.; David, W. I. F. Compositional flexibility in Li–N–H materials: implications for ammonia catalysis and hydrogen storage. *Phys. Chem. Chem. Phys.* **2021**, *23*, 15091–15100.

(19) Bramwell, P. L.; Lentink, S.; Ngene, P.; de Jongh, P. E. Effect of Pore Confinement of LiNH2 on Ammonia Decomposition Catalysis and the Storage of Hydrogen and Ammonia. *The Journal of Physical Chemistry C* **2016**, *120*, 27212–27220.

(20) Logadóttir, A.; Nørskov, J. Ammonia synthesis over a Ru(0001) surface studied by density functional calculations. *Journal of Catalysis* **2003**, *220*, 273–279.

(21) Honkala, K.; Hellman, A.; Remediakis, I. N.; Logadottir, A.; Carlsson, A.; Dahl, S.; Christensen, C. H.; Nørskov, J. K. Ammonia Synthesis from First-Principles Calculations. *Science* **2005**, *307*, 555–558.

(22) Herron, J. A.; Tonelli, S.; Mavrikakis, M. Atomic and molecular adsorption on Ru(0001). *Surface Science* **2013**, *614*, 64–74.

(23) Wittreich, G. R.; Liu, S.; Dauenhauer, P. J.; Vlachos, D. G. Catalytic resonance of ammonia synthesis by simulated dynamic ruthenium crystal strain. *Science Advances* **2022**, *8*, eabl6576.

(24) Mhadeshwar, A.; Kitchin, J.; Barteau, M.; Vlachos, D. The Role of Adsorbate–Adsorbate Interactions in the Rate Controlling Step and the Most Abundant Reaction Intermediate of NH3 Decomposition on Ru. *Catalysis Letters* **2004**, *96*, 13–22.

(25) Maier, S.; Stass, I.; Cerda, J. I.; Salmeron, M. Bonding of Ammonia and Its Dehydrogenated Fragments on Ru(0001). *The Journal of Physical Chemistry C* **2012**, *116*, 25395–25400.

(26) Lu, X.; Zhang, J.; Chen, W.-K.; Roldan, A. Kinetic and mechanistic analysis of NH3 decomposition on Ru(0001), Ru(111) and Ir(111) surfaces. *Nanoscale Adv.* **2021**, *3*, 1624–1632.

(27) Zhang, C.; Liu, Z.-P.; Hu, P. Stepwise addition reactions in ammonia synthesis: A first principles study. *The Journal of Chemical Physics* **2001**, *115*, 609–611.

(28) Zhang, C.; Lynch, M.; Hu, P. A density functional theory study of stepwise addition reactions in ammonia synthesis on Ru(0001). *Surface Science* **2002**, *496*, 221–230.

(29) Fan, Q.-Y.; Liu, J.-L.; Gong, F.-Q.; Wang, Y.; Cheng, J. Structural dynamics of Ru clusters during nitrogen dissociation in ammonia synthesis. *Phys. Chem. Chem. Phys.* **2022**, *24*, 10820–10825.

(30) Zhou, S.; Lin, S.; Guo, H. First-Principles Insights into Ammonia Decomposition Catalyzed by Ru Clusters Anchored on Carbon Nanotubes: Size Dependence and Interfacial Effects. *The Journal of Physical Chemistry C* **2018**, *122*, 9091–9100.

(31) Herbst, J. F.; Hector, L. G. Energetics of the Li amide/Li imide hydrogen storage reaction. *Phys. Rev. B* **2005**, *72*, 125120.

(32) Song, Y.; Guo, Z. X. Electronic structure, stability and bonding of the Li-N-H hydrogen storage system. *Phys. Rev. B* **2006**, *74*, 195120.

(33) Tsumuraya, T.; Shishidou, T.; Oguchi, T. First-principles study on lithium and magnesium nitrogen hydrides for hydrogen storage. *Journal of Alloys and Compounds* **2007**, *446-447*, 323–327.

(34) Wang, J.; Du, Y.; Xu, H.; Jiang, C.; Kong, Y.; Sun, L.; Liu, Z.-K. Native defects in $LiNH_2$: A first-principles study. *Phys. Rev. B* **2011**, *84*, 024107.

(35) Hoang, K.; Janotti, A.; Van de Walle, C. G. Mechanisms for the decomposition and dehydrogenation of Li amide/imide. *Phys. Rev. B* **2012**, *85*, 064115.

(36) Ning, H.; Lan, Z.; Bai, J.; Guo, J. Density function theory investigation on the thermodynamic properties of the Li–N–H system. *Materials Chemistry and Physics* **2014**, *144*, 484–490.

(37) Rajeswarapalanichamy, R.; Santhosh, M.; Sudhapriyanga, G.; Kanagaprabha, S.; Iyakutti, K. Structural Stability, Electronic Structure and Mechanical Properties of Li–N–H System. *Acta Metallurgica Sinica* **2015**, *28*, 550–558.

(38) Yamawaki, H.; Fujihisa, H.; Gotoh, Y.; Nakano, S. Structure of Intermediate Phase II of LiNH2 under High Pressure. *The Journal of Physical Chemistry B* **2014**, *118*, 9991–9996.

(39) Yang, J. B.; Zhou, X. D.; Cai, Q.; James, W. J.; Yelon, W. B. Crystal and electronic structures of LiNH2. *Applied Physics Letters* **2006**, *88*, 041914–041914.

(40) Miceli, G.; Cucinotta, C. S.; Bernasconi, M.; Parrinello, M. First Principles Study of the LiNH2/Li2NH Transformation. *The Journal of Physical Chemistry C* **2010**, *114*, 15174–15183.

(41) Kresse, G.; Hafner, J. Ab initio molecular dynamics for liquid metals. *Phys. Rev. B* **1993**, *47*, 558–561.

(42) Kresse, G.; Hafner, J. Ab initio molecular-dynamics simulation of the liquid-metal–amorphous-semiconductor transition in germanium. *Phys. Rev. B* **1994**, *49*, 14251–14269.

(43) Kresse, G.; Furthmüller, J. Efficiency of ab-initio total energy calculations for metals and semiconductors using a plane-wave basis set. *Computational Materials Science* **1996**, *6*, 15–50.

(44) Kresse, G.; Furthmüller, J. Efficient iterative schemes for ab initio total-energy calculations using a plane-wave basis set. *Phys. Rev. B* **1996**, *54*, 11169–11186.

(45) Perdew, J. P.; Burke, K.; Ernzerhof, M. Generalized Gradient Approximation Made Simple. *Phys. Rev. Lett.* **1996**, *77*, 3865–3868.

(46) Grimme, S.; Antony, J.; Ehrlich, S.; Krieg, H. A consistent and accurate ab initio parametrization of density functional dispersion correction (DFT-D) for the 94 elements H-Pu. *The Journal of Chemical Physics* **2010**, *132*, 154104.

(47) Grimme, S.; Ehrlich, S.; Goerigk, L. Effect of the damping function in dispersion corrected density functional theory. *Journal of Computational Chemistry* **2011**, *32*, 1456–1465.

(48) Steinmann, S. N.; Corminboeuf, C. A generalized-gradient approximation exchange hole model for dispersion coefficients. *The Journal of Chemical Physics* **2011**, *134*, 044117.

(49) Steinmann, S. N.; Corminboeuf, C. Comprehensive Benchmarking of a Density-Dependent Dispersion Correction. *Journal of Chemical Theory and Computation* **2011**, *7*, 3567–3577.

(50) Kresse, G.; Joubert, D. From ultrasoft pseudopotentials to the projector augmented-wave method. *Phys. Rev. B* **1999**, *59*, 1758–1775.

(51) Henkelman, G.; Arnaldsson, A.; Jónsson, H. A fast and robust algorithm for Bader decomposition of charge density. *Computational Materials Science* **2006**, *36*, 354–360.

(52) Sanville, E.; Kenny, S. D.; Smith, R.; Henkelman, G. Improved grid-based algorithm for Bader charge allocation. *Journal of Computational Chemistry* **2007**, *28*, 899–908.

(53) Tang, W.; Sanville, E.; Henkelman, G. A grid-based Bader analysis algorithm without lattice bias. *Journal of Physics: Condensed Matter* **2009**, *21*, 084204.

(54) Arblaster, J. W. Crystallographic Properties of Ruthenium. *Platinum Metals Review* **2013**, *57*, 127–136.

(55) Jacobs, H.; Juza, R. Neubestimmung der Kristallstruktur des Lithiumamids. *Zeitschrift für anorganische und allgemeine Chemie* **1972**, *391*, 271–279.

(56) Lin, H.-J.; Zhang, P.; Fang, Y.-X.; Zhao, Y.-J.; Zhong, H.; Tang, J.-J. Understanding the Decomposition Mechanisms of LiNH2, Mg(NH2)2, and NaNH2: A Joint Experimental and Theoretical Study. *The Journal of Physical Chemistry C* **2019**, *123*, 18180–18186.

(57) Janthon, P.; Luo, S. A.; Kozlov, S. M.; Vines, F.; Limtrakul, J.; Truhlar, D. G.; Illas, F. Bulk Properties of Transition Metals: A Challenge for the Design of Universal Density Functionals. *Journal of Chemical Theory and Computation* **2014**, *10*, 3832–3839.

(58) Chen, P.; Xiong, Z.; Luo, J.; Lin, J.; Tan, K. L. Interaction of hydrogen with metal nitrides and imides. *Nature* **2002**, *420*, 302–304.

(59) Ebinger, H.; Arnolds, H.; Polenz, C.; Polivka, B.; Preyß, W.; Veith, R.; Fick, D.; Jänsch, H. Adsorption and diffusion of Li on an Ru(001) surface: an NMR study. *Surface Science* **1998**, *412-413*, 586–615.

(60) Mannstadt, W.; Freeman, A. J. LDA theory of the coverage dependence of the local density of states: Li adsorbed on Ru(001). *Phys. Rev. B* **1998**, *57*, 13289–13294.

(61) Mannstadt, W. Coverage dependence of the work function of Li adsorbed on Ru(001): ab initio studies within DFT. *Surface Science* **2003**, *525*, 119–125.

(62) Tyson, W. R.; Miller, W. A. Surface free energies of solid metals: Estimation from liquid surface tension measurements. *Surface Science* **1977**, *62*, 267–276.

TOC Graphic

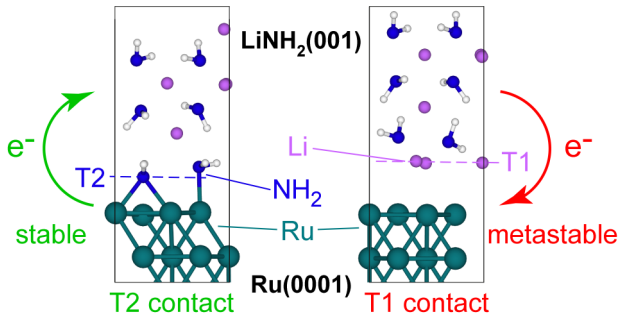
LiNH2(001)
e-
T2
NH2
Li
T1
e-
stable
Ru
metastable
Ru(0001)
T2 contact
T1 contact

Table 1: Ground-state structural and energetic properties of optimized ruthenium and lithium amide bulks predicted by DFT calculations with various exchange and correlation functionals : pure GGA PBE, and dispersion-corrected PBE-D3(0D), PBE-D3(BJ), PBE-dDsC. Those optimized bulks are non magnetic. Lattice parameters (a, c, Å), cohesion energy (E_{coh}, eV/at.), formation energy (E_{form}, eV/$LiNH_2$), bulk modulus (B_0, GPa) and its derivative (B'_0, dimensionless). Experimental crystallographic and energetic data are also reported.

System	Ru Bulk					$LiNH_2$				
Functional	GGA PBE	DFT-D3 PBE(0D)	DFT-D3 PBE(BJ)	dDsC PBE	Exp.	GGA PBE	DFT-D3 PBE(0D)	DFT-D3 PBE(BJ)	dDsC PBE	Exp.
a (Å)	2.71(5)	2.69(2)	2.69(2)	2.70(1)	2.7059[a]	5.00(4)	4.89(8)	4.85(1)	4.85(2)	5.0344[b]
c (Å)	4.28(0)	4.24(8)	4.25(0)	4.26(2)	4.2815[a]	10.32(5)	10.13(1)	10.07(6)	10.13(4)	10.2556[b]
E_{coh} (eV/at.)	-7.19(4)	-7.75(3)	-7.75(0)	-7.56(4)	-6.74[c]	-3.36(0)	-3.38(0)	-3.40(7)	-3.36(9)	
E_{form} (eV)						-2.07(4)	-2.05(8)	-2.09(3)	-2.07(0)	-1.82[d]
B_0 (GPa)	310	311	312	311	303[c]	24	30	31	30	
B'_0	4.8	4.7	4.6	4.7		4.8	4.9	4.9	4.1	

[a] see Ref.[54] [b] see Ref.[39] [c] see Ref.[57] [d] see Ref.[58]

Table 2: Surface energies (J.m^{-2}) and magnetization (μ_B) of optimized Ru(0001) (7 atomic layers) and $LiNH_2$(001) (from 23 to 25 planes) clean slabs according to pure GGA PBE and dispersion-corrected PBE-dDsC functionals. For $LiNH_2$(001), the four possible terminations (T_i) can be combined into two stoichiometric, neutral and pristine mixed slabs (T1T3 and T3T4) or four non stoichiometric, polar and pristine symmetric systems (T1T1, T2T2, T3T3 and T4T4).

System	Surface energy			Magnetization	
Functional	GGA PBE	PBE-dDsC	Refs.	GGA PBE	PBE-dDsC
Ru(0001)	2.59(6)	3.02(2)	2.65[a]	-	-
$LiNH_2$(001)-T1T2	5.00(7)	5.57(4)		2.73(5)	1.64(6)
$LiNH_2$(001)-T3T4	1.45(6)	1.83(0)		0.37(7)	0.37(9)
$LiNH_2$(001)-T1T1	4.77(3)	5.17(7)		2.77(2)	1.64(5)
$LiNH_2$(001)-T2T2	0.35(4)	0.48(9)		-3.00(0)	3.00(0)
$LiNH_2$(001)-T3T3	1.53(5)	1.73(1)		0	0
$LiNH_2$(001)-T4T4	0.01(5)	0.20(8)		0.99(8)	0.99(8)

[a] Exp. Ref.[62]

Table 3: Adsorption properties of Li atom and NH_2 fragment on Ru(0001) (GGA PBE, coverage 0.25 ML): adsorption site, energy E_{ads} (eV), key distances (Å).

System	Li					NH_2	
Site	Top	Bridge	Hollow HCP	Hollow free	Refs.	Bridge	Refs.
E_{ads} (eV)	-2.33	-2.50	-2.53	-2.53	-2.5[a]	-2.97	-2.95[d]; -3.01[e]
Ru-Li (Å)	2.42	2.62	2.71	2.71	2.22[b]; 2.13[c]		
Ru-N (Å)						2.12(2)	2.13[d,f]
N-H (Å)						1.02(1)	1.015[d,f]

[a] Experimental for a surface coverage of 0.020 ML [59]
[b] LDA calculation at a coverage of 0.25 ML [60]
[c] LDA calculation at a coverage of 0.25 ML [61]
[d] GGA B88XP86C calculation at a coverage of 1/6 ML [28]
[e] GGA PW91 at a coverage of 0.25 ML [22]
[f] GGA rPBE at a coverage of 1/16 ML [26]

Table 4: Interface name, interface energy ($J.m^{-2}$), total magnetization (μB) and energy decomposition analysis (sum of surface energies of separated materials and adhesion energies between them, all expressed in $J.m^{-2}$) for all the DFT models of Ru(0001)/$LiNH_2$(001) system (GGA PBE and PBE-dDsC functionals). Reconstructions of the $LiNH_2$(001) structure are mentioned with the corresponding transformations for terminal planes, when they occurred during the geometry optimizations.

Interface	Structure	Interface energy		Magnetization		Sum of surface energies		Adhesion energy	
Functional	Reconstruction	GGA PBE	PBE-dDsC	GGA PBE	PBE-dDsC	GGA PBE	PBE-dDsC	GGA PBE	PBE-dDsC
Ru@T1T4(10,ns,nz,ps)	none	7.36(6)	-	0.32(0)	-	10.06(7)	-	-2.70(1)	-
Ru@T1T4(14,ns,nz,ps)	none	7.50(1)	-	0	-	10.06(7)	-	-2.56(7)	-
Ru@T1T3(11,ns,p,ps)	none	9.14(5)	-	0	-	11.58(8)	-	-2.44(2)	-
Ru@T1T3(15,ns,p,ps)	none	9.21(7)	-	0	-	11.58(8)	-	-2.37(1)	-
Ru@T1T2(12,s,n,ps)	$T1T2 \rightarrow T1T4'$	7.09(8)	-	1.34(1)	-	10.40(6)	-	-3.30(8)	-
Ru@T1T2(16,s,n,ps)	$T1T2 \rightarrow T1T4'$	7.21(4)	-	1.39(0)	-	10.40(6)	-	-3.19(2)	-
Ru@T1T1(13,ns,p,ps)	none	12.24(0)	-	0	-	14.82(1)	-	-2.58(1)	-
Ru@T1T1(17,ns,p,ps)	none	12.30(5)	-	0.08(3)	-	14.82(1)	-	-2.51(6)	-
Ru@T1T3(11,s,nz,2vLi(int))	$T3T3 \rightarrow T56T43$	5.83(8)	-	0	-	11.58(8)	-	-5.75(0)	-
Ru@T1T3(11,s,nz,2vLi(cor))	$T1T3 \rightarrow T1T3$	7.23(5)	-	1.13(4)	-	11.58(8)	-	-4.35(2)	-
Ru@T1T3(15,s,nz,2vLi(int))	$T3T3 \rightarrow T56T3$	6.32(7)	-	-0.07(9)	-	11.58(8)	-	-5.26(0)	-
Ru@T1T1(13,s,nz,3vLi(int,cor,suf))	$T5T5 \rightarrow T36T4'3$	5.96(6)	-	-0.0002	-	14.82(1)	-	-8.85(5)	-
Ru@T1T1(17,s,nz,3vLi(int,2cor))	$T5T1 \rightarrow T36T4'3$	7.46(7)	-	0	-	14.82(1)	-	-7.97(4)	-
Ru@T2T4(9,ns,nz,ps)	none	2.37(3)	2.66(6)	-0.30(3)	-0.32(0)	5.65(2)	6.62(5)	-3.28(0)	-3.96(9)
Ru@T2T4(13,ns,nz,ps)	none	2.50(4)	2.17(7)	0.35(7)	0.37(3)	5.65(2)	6.62(5)	-3.14(8)	-4.44(8)
Ru@T2T3(10,ns,p,ps)	$T2T3 \rightarrow T23T3$	4.10(2)	4.23(9)	0	0	7.17(3)	7.93(3)	-3.07(5)	-3.69(4)
Ru@T2T3(14,ns,p,ps)	none	4.23(0)	3.70(5)	0	0	7.17(3)	7.93(3)	-2.94(3)	-4.22(7)
Ru@T2T2(11,ns,p,ps)	$T2T2 \rightarrow T2T4'$	1.93(2)	2.04(2)	0.58(7)	0	5.99(1)	6.75(1)	-4.05(9)	-4.70(9)
Ru@T2T2(15,ns,p,ps)	$T2T2 \rightarrow T2T4'$	2.23(0)	1.92(5)	1.37(6)	1.41(5)	5.99(1)	6.75(1)	-3.76(1)	-4.82(7)
Ru@T2T1(12,s,n,ps)	$T2T1 \rightarrow T23T65$	7.02(5)	6.84(2)	-0.19(0)	0	10.40(6)	11.17(0)	-3.38(1)	-4.32(9)
Ru@T2T1(16,s,n,ps)	$T2T1 \rightarrow T2T65$	7.08(8)	6.26(7)	0.07(8)	0	10.40(6)	11.17(0)	-3.31(8)	-4.90(3)
Ru@T2T3(10,ns,nz,vLi(cor))	$T2T3 \rightarrow T2T43$	2.42(3)	2.79(3)	0	0	7.17(3)	7.93(3)	-4.75(0)	-5.14(0)
Ru@T2T3(14,ns,nz,vLi(cor))	none	3.08(7)	2.84(7)	-0.10(6)	0	7.17(3)	7.93(3)	-4.08(5)	-3.35(2)
Ru@T2T2(11,ns,nz,vNH_2(cor))	$T2T2 \rightarrow T2T4'$	3.13(2)	3.43(3)	0.51(7)	0	5.99(1)	6.75(1)	-2.85(9)	-3.31(8)
Ru@T2T2(11,ns,nz,vNH_2(suf))	$T2T2 \rightarrow T2T4'$	2.65(8)	2.86(6)	-0.37(2)	0	5.99(1)	6.75(1)	-3.33(3)	-3.88(5)

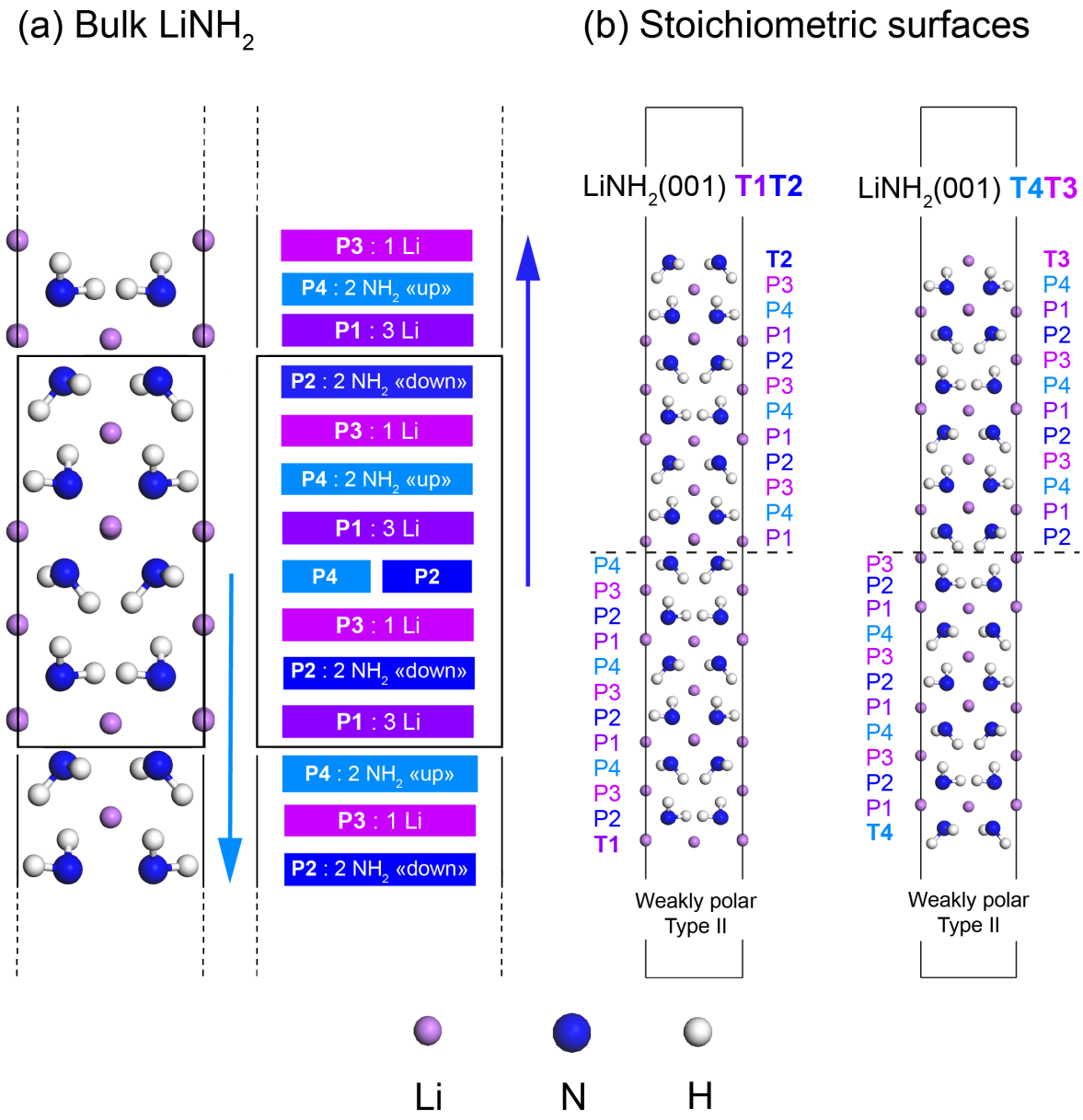

Figure 1: (a) Definitions and notations related to the four planes (P_i, $i = 1, ..., 4$) in the bulk of $LiNH_2$ materials leading to the generation of four surface terminations for $LiNH_2(001)$ (noted T_i, $i = 1, ..., 4$, respectively). Please note that in our lateral view, two of the three Li atoms of P1 plane are superposed. In the bulk, the notations of the Li and NH_2 planes are symmetrized starting from a hypothetic central NH_2 plane, in order to be able to define the equivalent planes in the symmetric slabs of $LiNH_2(001)$, by following the blue arrows. (b) Bulk truncated structures of the two possible stoichiometric, neutral and pristine terminations for the $LiNH_2(001)$ surface. According to our notations, the T2 termination corresponds to a surface composed of NH_2 fragments pointing toward $LiNH_2$ materials ("NH_2 down"), whereas, in T4 termination, the surface NH_2 moieties are pointing toward vacuum ("NH_2 up"). The notations of the different planes are following the definitions of the bulk exposed in (a). Labels and colors of atoms are depicted.

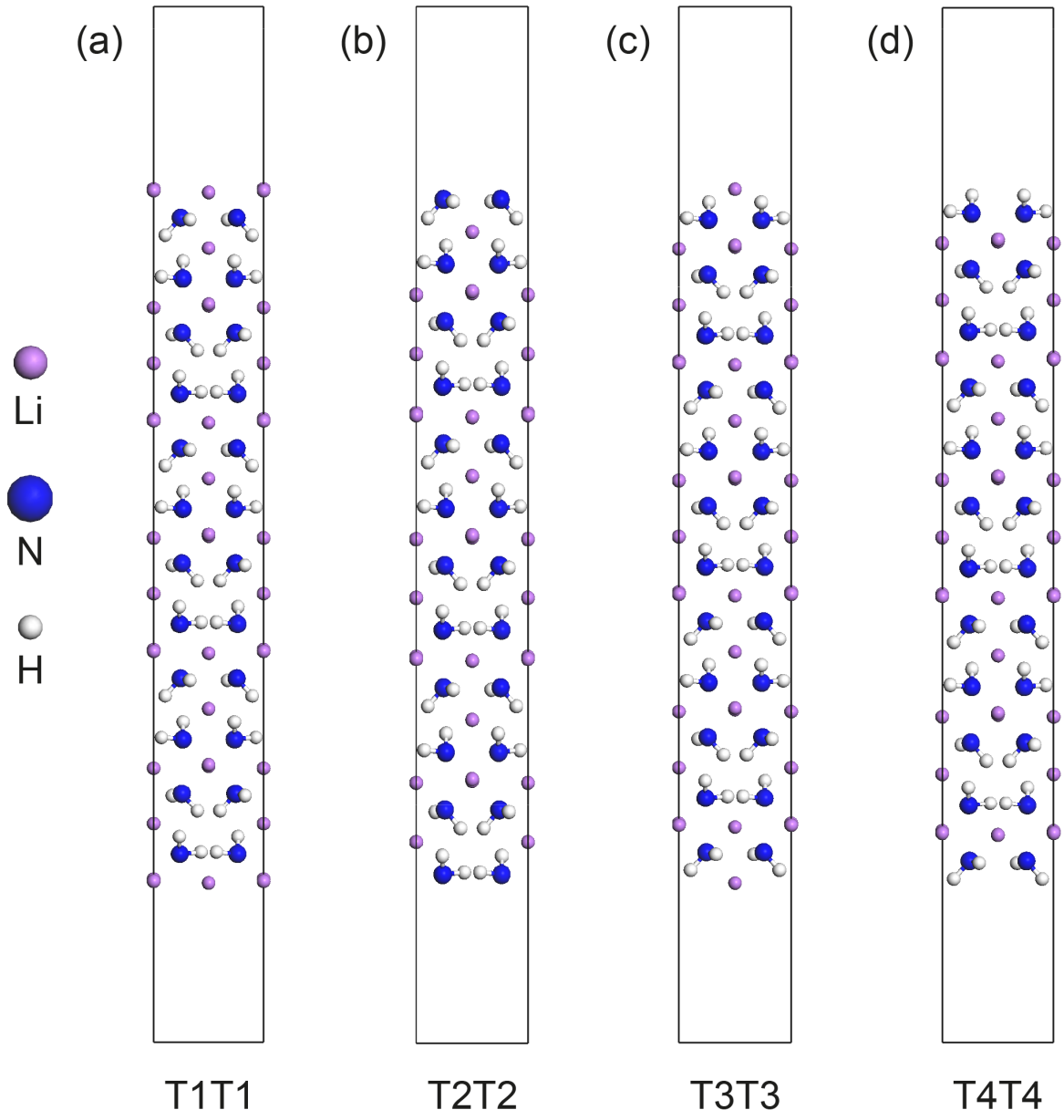

Figure 2: Lateral views of the four possible bulk truncated symmetric and unrelaxed models of non stoichiometric, polar and pristine $LiNH_2(001)$ surfaces: (a) T1T1, (b) T2T2, (c) T3T3, (d) T4T4 terminations. Labels and colors of atoms are depicted.

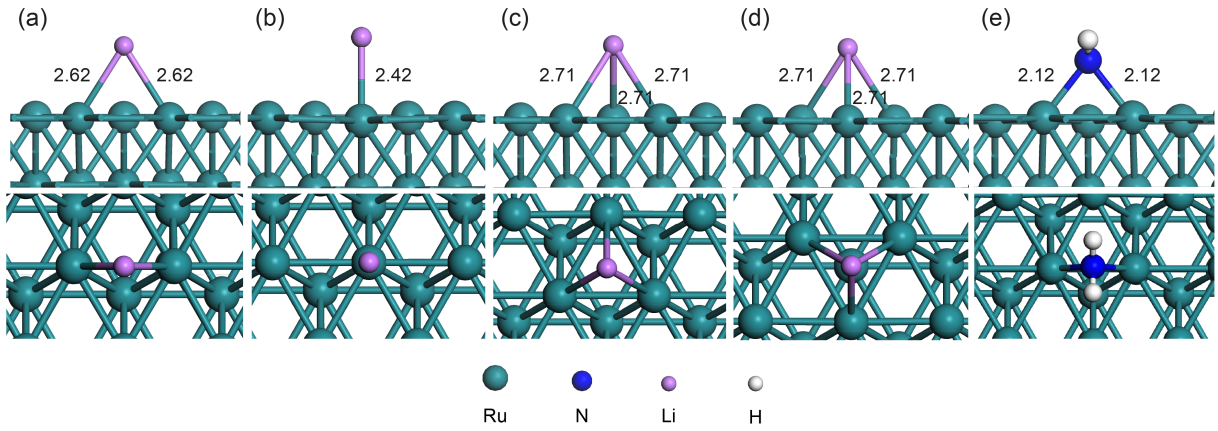

Figure 3: Lateral and top views of optimized adsorption structures of a Li atom on Ru(0001): (a) bridge, (b) top, (c) hollow free and (d) hollow hcp positions. (e) Lateral and top views of the optimal adsorption structure of a bridge-bonded NH_2 fragment on Ru(0001). Distances are addressed in Å. Labels and colors of atoms are depicted.

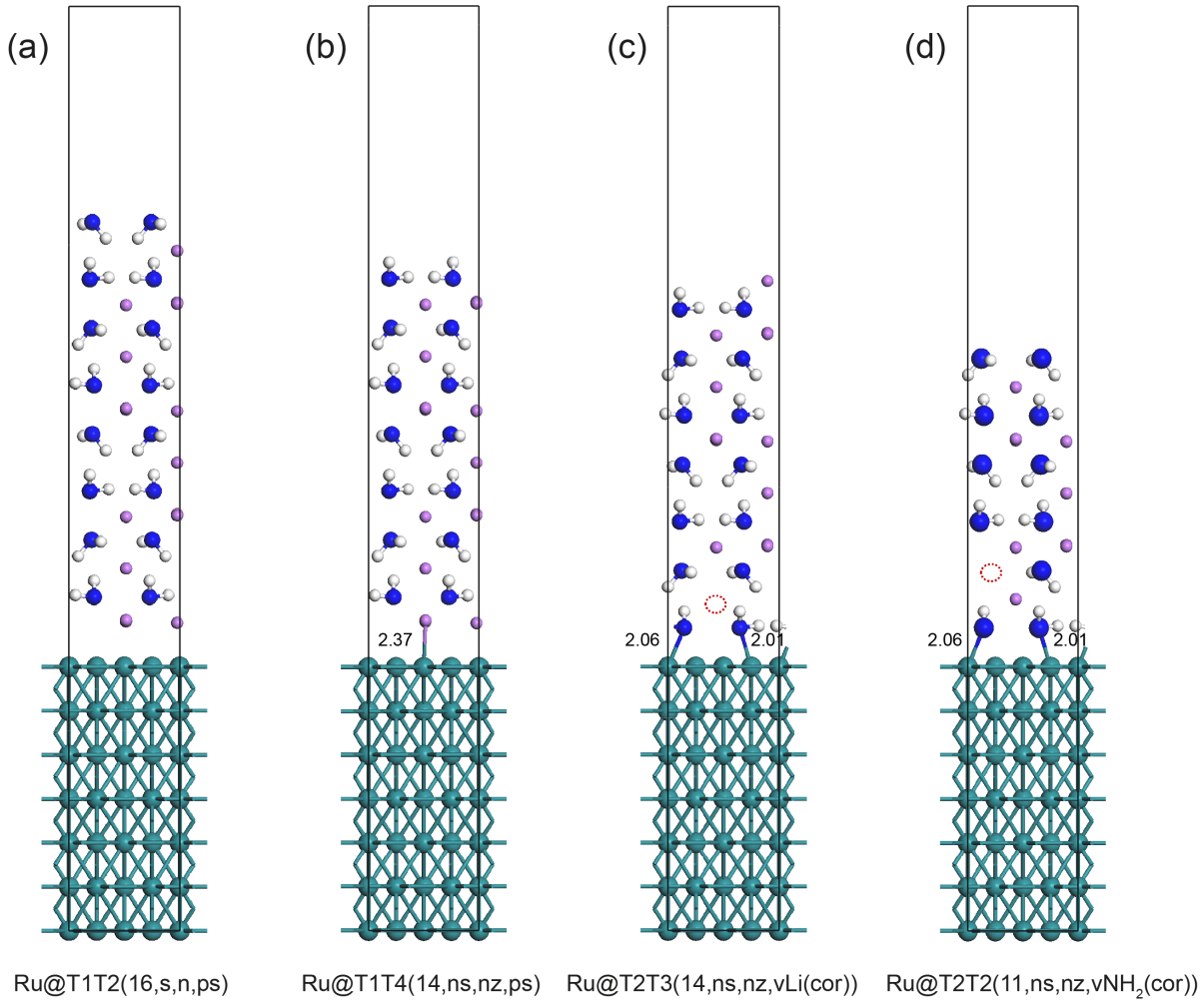

Figure 4: Lateral views of starting geometries of Ru(0001)/$LiNH_2$(001) typical interfaces. A $(2 \times \sqrt{3})$ supercell is chosen to minimize the materials structural mismatch: (a) stoichiometric (s), neutral (n) and pristine (ps) Ru@T1T2(16,s,n,ps) interface (composed of 16 layers of $LiNH_2$); (b) non-stoichiometric (ns), neutralized (nz) and pristine Ru@T1T4(14,ns,nz,ps) interface (composed of 14 layers of $LiNH_2$); (c) non-stoichiometric, neutralized and defective Ru@T2T3(14,ns,nz,vLi(cor)) interface (with a single Li vacancy in the core, noted vLi(cor), of 14 layers of $LiNH_2$); (d) stoichiometric, neutralized and defective Ru@T2T2(11,ns,nz,vNH_2(cor)) interface (with a single NH_2 vacancy in the core, noted vNH_2(cor), of 11 layers of $LiNH_2$). Single vacancies are marked by red dotted line circles. Distances are expressed in Å. The colors and atom labels are those depicted in previous Figures 1-3.

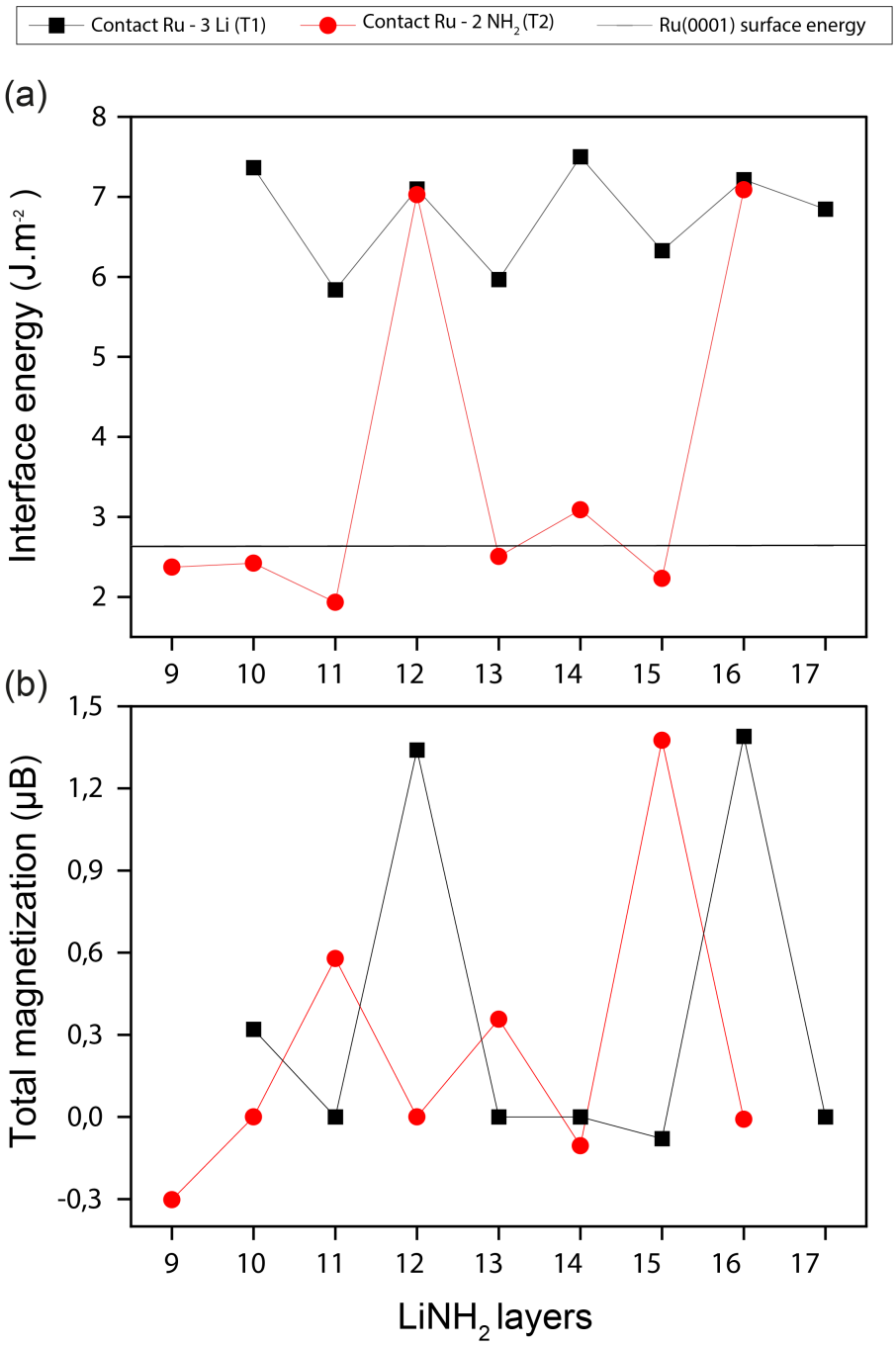

Figure 5: (a) Interface energies ($J.m^{-2}$) of optimized Ru(0001)/$LiNH_2$(001) systems (GGA PBE) as a function of the thickness of $LiNH_2$(001) slab (see Table 4 for details). The two considered contacts between materials is marked by different colors : black for a contact with an atomic Li plane P1 (related to T1 termination) and red for a contact with a NH_2 molecular plane P2 (related to T2 termination). See Figure 1 for definitions of planes in $LiNH_2$. For a given thickness, only the interface energy of the most stable model is reported from Table 4. The horizontal black line corresponds to the calculated value of the surface energy of the clean reference Ru(0001). (b) Total magnetization (μB) of optimized Ru(0001)/$LiNH_2$(001) interfaces (GGA PBE) as a function of the thickness of $LiNH_2$(001) slab.

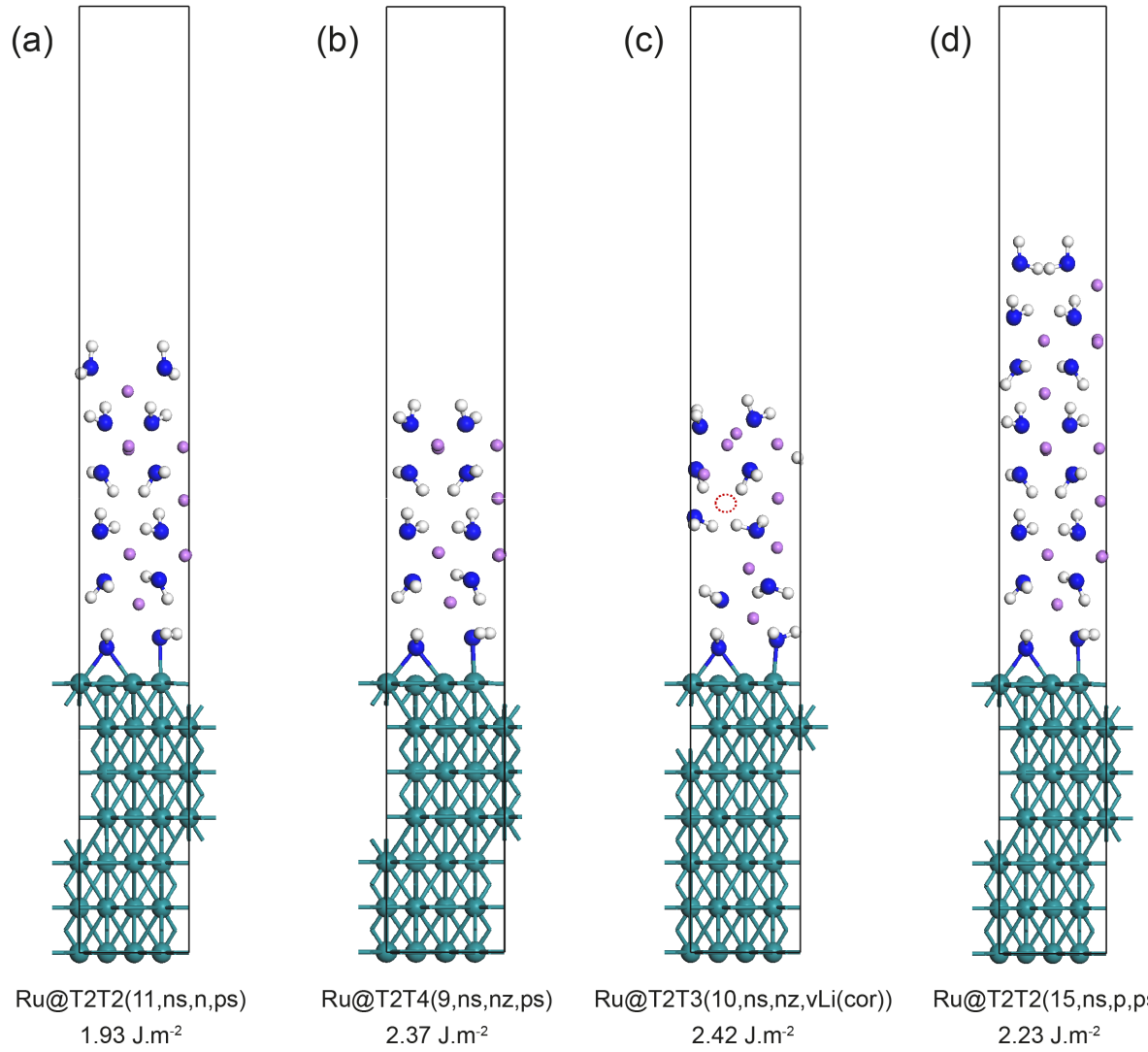

Figure 6: Lateral views of optimized structures of Ru(0001)/$LiNH_2$(001) most stable interfaces (GGA PBE): (a) non-stoichiometric (ns), polar (p) and pristine (ps) Ru@T2T2(11,ns,p,ps) reconstructed interface (composed of 11 layers of $LiNH_2$ reconstructed in $T2T4'$); (b) non-stoichiometric, neutralized (nz) and pristine Ru@T2T4(9,ns,nz,ps) interface (composed of 9 layers of $LiNH_2$); (c) non-stoichiometric, neutralized and defective Ru@T2T3(10,ns,nz,vLi(cor)) reconstructed interface (with a single Li vacancy in the core, noted vLi(cor), of 10 layers of $LiNH_2$ reconstructed in $T2T43$); (d) non-stoichiometric, polar and pristine Ru@T2T2(15,ns,p,ps) reconstructed interface (composed of 15 layers of $LiNH_2$ reconstructed in $T2T4'$). Single vacancies are marked by red dotted line circles. Interface energies are expressed in J.m^{-2}. The colors and atom labels are those depicted in previous Figures 1-3.

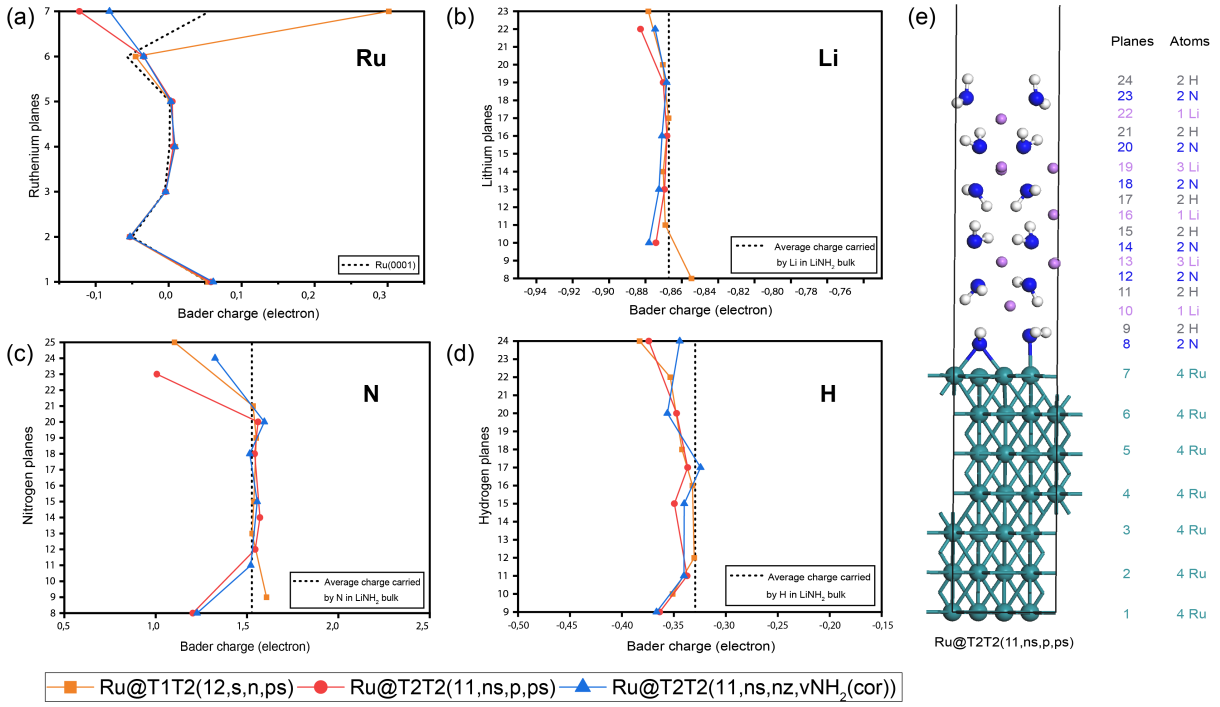

Figure 7: Bader transfer charge transfer analysis of separate Ru(0001), $LiNH_2$ bulk systems (black dotted lines) and Ru@T2T2(11,ns,p,ps) (red full line), Ru@T2T2(11,ns,nz,vNH_2(cor)) (blue full line) and Ru@T1T2(12,s,n,ps) (orange full line) interfaces. The chosen pristine Ru@T2T2(11,ns,p,ps) and Ru@T1T2(12,s,n,ps) interfaces are the most stable ones through a T2 or a T1 contact with $LiNH_2$, respectively. The selected defective Ru@T2T2(11,ns,nz,vNH_2(cor)) interface presents the influence of a single NH_2 vacancy in the core of $LiNH_2$ materials on the Bader charge transfer. (a) layer by layer average Bader charge per Ru atom in the Ru(0001) seven-layer slab, in presence or in absence of the contact with $LiNH_2$; (b) layer by layer average Bader charge per Li atom in the Li atomic planes of $LiNH_2$, in presence or in absence of the contact with Ru(0001); (c) layer by layer average Bader charge per N atom in the NH_2 planes of $LiNH_2$, in presence or in absence of the contact with Ru(0001); (d) layer by layer average Bader charge per H atom in the NH_2 planes of $LiNH_2$, in presence or in absence of the contact with Ru(0001); (e) an example of the definitions of the planes is given in the structure illustrating the most stable interface Ru@T2T2(11,ns,p,ps). In our definition, the Bader charges are calculated by taking the valence of the isolated atoms as references. Ru atoms exhibit positive or negative Bader charges meaning that they can be either negatively or positively charges, respectively. N atoms of $LiNH_2$ present systematically positive Bader charges meaning they are negatively charged. At the opposite, Li and H atoms of $LiNH_2$ are always positively charged.